

Impact of ejecta morphology and composition on the electromagnetic signatures of neutron star mergers

Ryan T. Wollaeger¹, Oleg Korobkin¹,^{*} Christopher J. Fontes¹, Stephan K. Rosswog², Wesley P. Even^{1,3}, Christopher L. Fryer^{1,4,5}, Jesper Sollerman², Aimee L. Hungerford¹, Daniel R. van Rossum⁶, and Allan B. Wollaber¹

¹Center for Theoretical Astrophysics, Los Alamos National Laboratory, Los Alamos, NM 87545, USA

²The Oskar Klein Centre, Department of Astronomy, AlbaNova, Stockholm University, SE-106 91 Stockholm, Sweden

³Southern Utah University, Cedar City, UT 84720, USA

⁴University of New Mexico, Albuquerque, NM 87131, USA

⁵University of Arizona, Tucson, AZ 85721, USA

⁶Radboud Radio Lab, Radboud University, Nijmegen, Netherlands

Last updated 14 March 2018

ABSTRACT

The electromagnetic transients accompanying compact binary mergers (γ -ray bursts, afterglows and ‘macronovae’) are crucial to pinpoint the sky location of gravitational wave sources. Macronovae are caused by the radioactivity from freshly synthesised heavy elements, e.g. from dynamic ejecta and various types of winds. We study macronova signatures by using multi-dimensional radiative transfer calculations. We employ the radiative transfer code SuperNu and state-of-the-art LTE opacities for a few representative elements from the wind and dynamical ejecta (Cr, Pd, Se, Te, Br, Zr, Sm, Ce, Nd, U) to calculate synthetic light curves and spectra for a range of ejecta morphologies. The radioactive power of the resulting macronova is calculated with the detailed input of decay products. We assess the detection prospects for our most complex models, based on the portion of viewing angles that are sufficiently bright, at different cosmological redshifts (z). The brighter emission from the wind is unobscured by the lanthanides (or actinides) in some of the models, permitting non-zero detection probabilities for redshifts up to $z = 0.07$. We also find the nuclear mass model and the resulting radioactive heating rate are crucial for the detectability. While for the most pessimistic heating rate (from the FRDM model) no reasonable increase in the ejecta mass or velocity, or wind mass or velocity, can possibly make the light curves agree with the observed nIR excess after GRB130603B, a more optimistic heating rate (from the Duflo-Zuker model) leads to good agreement. We conclude that future reliable macronova observations would constrain nuclear heating rates, and consequently help constrain nuclear mass models.

Key words: neutron stars, mergers, electromagnetic counterparts, gravitational waves

1 INTRODUCTION

Neutron star mergers (NSMs) realize extreme conditions, probing the limits of fundamental theories. The matter evolves in a curved space-time at several times nuclear density and at temperatures in excess of 10^{11} K. Moreover, the high density and curved space-time have the potential to generate magnetic fields beyond magnetar strength. These events announce themselves through a variety of channels: electromagnetic, gravitational, nucleosynthetic signatures and even neutrinos in the (un-)lucky occurrence of a nearby event. The most conspicuous signatures of NSMs are thought to be short

γ -ray bursts (GRBs, see Popham et al. 1999; Fryer et al. 1999; Bloom et al. 1999; Piran 2005; Lee & Ramirez-Ruiz 2007; Nakar 2007; Fong & Berger 2013; Berger 2014), and it is very likely that advanced detector facilities such as AdLIGO (The LIGO Scientific Collaboration et al. 2015), Advanced VIRGO (Acernese et al. 2015) and KAGRA (Akutsu & the KAGRA Collaboration 2015), will also detect the long-awaited NSM gravitational wave signals.

In a NSM several physical mechanisms conspire to unbind material from the merging stars, releasing neutron-rich outflows into the surrounding galactic environment. The NSM outflows can be subdivided into several classes according to their ejecta amounts, neutron richness, morphologies, and expansion velocities. First, the *dynamical ejecta* are expelled by gravity, centrifugal and pressure

* email: korobkin@lanl.gov

forces at the moment of the merger itself. Numerical simulations indicate that this type of outflow has velocities in the subrelativistic regime $\sim 0.1 - 0.3 c$, is very neutron-rich ($Y_e \sim 0.03 - 0.2$), and has masses in the range $\sim 10^{-4} - 0.05 M_\odot$ (Rosswog 2013; Bauswein et al. 2013; Hotokezaka et al. 2013; Sekiguchi et al. 2016; Lehner et al. 2016; Rosswog et al. 2017; Endrizzi et al. 2016). If the collapse to a black hole (BH) is delayed, an intense *neutrino- and accretion-driven wind* is launched from the hot surface of the resulting hypermassive neutron star (HMNS, Dessart et al. 2009; Perego et al. 2014; Just et al. 2015; Martin et al. 2015). This wind has a higher electron fraction $Y_e \sim 0.3 - 0.5$, but lower velocity and mass. Additional outflow can be launched from the HMNS by the strong magnetic fields (Siegel et al. 2014; Cioffi & Siegel 2015). Finally, nuclear recombination assisted by viscous magnetic forces unbinds outer layers of the post-merger accretion disk and launches *disk wind* outflows (Chen & Beloborodov 2007; Metzger et al. 2008; Fernández & Metzger 2013; Just et al. 2015). The disk winds have estimated velocities $v \sim 0.05 - 0.1 c$, moderately neutron rich composition with electron fraction $Y_e \sim 0.2 - 0.4$ and a mass comparable to that of dynamical ejecta. A fair pictorial representation of NSM outflows can be found e.g. in Rosswog (2013). If scientists can observationally distinguish the wind mass loss for systems that spend more than 100 ms as HMNSs versus those that collapse quickly to a BH, they can probe the equation of state of dense matter (Fryer et al. 2015).

It has been suggested that the neutron-rich outflows from NSMs can be important sites for the "strong" *r*-process nucleosynthesis (Lattimer & Schramm 1974; Lattimer et al. 1977; Eichler et al. 1989; Freiburghaus et al. 1999)¹. This hypothesis has attracted much attention recently, after attempts to robustly produce heavy *r*-process elements in core-collapse supernova simulations encountered significant difficulties (Arcones et al. 2007; Fischer et al. 2010; Roberts et al. 2010; Thielemann et al. 2011). Other indirect observational evidence also points to a rare, robust event (such as a NSM) as the main "strong" *r*-process producer: the robust pattern of abundances in old metal-poor *r*-process stars (Snedden et al. 2008), the absence of any traces of recent ²⁴⁴Pu in deep sea reservoirs (Turner et al. 2004; Wallner et al. 2015; Hotokezaka et al. 2015b), and the newly discovered "*r*-process galaxy" in the family of ultra-faint dwarf galaxies (Ji et al. 2015; Hirai et al. 2015).

Residual *r*-process radioactivity can potentially power an electromagnetic transient, a so-called "macronova" (or "kilonova", see Metzger 2016, for discussion of the naming conventions). This idea was originally proposed in Li & Paczyński (1998), revived in Kulkarni (2005) and further developed in Metzger et al. (2010); Metzger & Berger (2012). The opacities adopted for dynamical ejecta in these early works were seriously underestimated and led to overly optimistic prediction for detectability. Macronova detection prospects became dimmer after it was realized that the opacities in the optical and near infrared are a few orders of magnitude higher due to heavy line blanketing by lanthanides (Kasen et al. 2013; Barnes & Kasen 2013; Fontes et al. 2015a, 2017). Subsequent studies (Grossman et al. 2014; Rosswog et al. 2014; Kyutoku et al. 2013; Metzger & Fernández 2014) including detailed radiative transfer simulations (Tanaka & Hotokezaka 2013; Tanaka et al. 2014; Kasen et al. 2015) with updated opacities predicted dimmer light curves that would

peak after a few days in the infrared part of the spectrum, implying more pessimistic prospects for macronova detection.

Despite these difficulties, as of now, several candidate kilonova/macronova events have been identified (Tanvir et al. 2013; de Ugarte Postigo et al. 2014; Berger et al. 2013; Yang et al. 2015; Jin et al. 2015), but their nature is still very ambiguous due to sparse observational data and uncertainties in theoretical models. These uncertainties include the partition of radioactive energy between different decay products, which then have different capacities for thermalization (Hotokezaka et al. 2015a; Barnes et al. 2016). The influence of the radioactive heating rates was studied by Lippuner & Roberts (2015), who found that the heating profile remains quite featureless (see also Barnes et al. 2016; Rosswog et al. 2017; Wu et al. 2016). Barnes et al. (2016) explored four different nuclear mass models and analysed thermalization in detail. Their results show that the uncertainty in thermalization has a sub-dominant effect on light curves relative to the theoretical uncertainty in the nuclear mass model (see their Fig.17).

Detection of electromagnetic counterparts would provide crucial information to localize the astrophysical environments of gravitational wave signals (Metzger & Berger 2012; Nissanke et al. 2013; Piran et al. 2013; Singer et al. 2014; Chu et al. 2015; Ghosh et al. 2015; Bartos et al. 2016; Abbott et al. 2016a). Preliminary searches for the electromagnetic macronova-like transients following gravitational wave candidate triggers (e.g. Aasi et al. 2014; Copperwheat et al. 2016) were not successful in finding plausible candidates, and neither was a recent search in the dark energy surveys (Doctor et al. 2017). Additionally, nearby short GRBs (GRB160314A, GRB160821B) did not exhibit clear signs of bright macronovae (Kasliwal et al. in prep, Troja et al. in prep). These non-detections indicate that many macronovae are indeed as faint as predicted, possibly due to the high opacity of lanthanides and the low ejected mass (relative to supernovae). Recent comprehensive reviews of electromagnetic counterparts can be found in Rosswog (2015b), Fernández & Metzger (2015) and Metzger (2016).

Thus, accurate and reliable macronova light curve predictions are needed to constrain the detection prospects of NSMs. Previous studies with detailed multidimensional radiative transfer (Kasen et al. 2013; Barnes & Kasen 2013; Tanaka & Hotokezaka 2013; Tanaka et al. 2014; Kasen et al. 2015; Fernández et al. 2016; Barnes et al. 2016) used the Sobolev expansion opacity formalism to treat the substantial number of lines that can occur in the spectra of lanthanide and actinide elements. In the present work, we consider an alternative line-smearing approach that conserves the integral of the opacity over frequency (Fontes et al. 2015a, 2017). The latter method can produce significantly higher opacities compared to the expansion opacity formalism. In this study, we extend the work of Fontes et al. (2015a, 2017) with a state-of-the art open source radiative transfer code, SuperNu² (Wollaeger & van Rossum 2014), which implements a 3D semi-implicit multigroup Monte Carlo solver. With SuperNu and the line-smearing opacities, we explore the effects of varying NSM ejecta morphology, composition (or opacity), and *r*-process decay heating on macronova light curves and spectra.

The morphology of the outflow from a NSM depends on the binary mass ratio and the nuclear equation of state. Tidal dynamical ejecta, which are expelled from the system on a dynamical merger timescale, tend to preserve a quasi-toroidal configuration. On the other hand, general relativistic simulations with soft equations of state show highly irregular hot outflows from the shocked interface,

¹ However, see Côté et al. (2017) for a literature review and a recent critical discussion of *r*-process sites from the perspective of chemical evolution and population synthesis modelling.

² <https://bitbucket.org/drrossum/supernu/wiki/Home>

which become almost isotropic. Here, we explore both a sequence of toroidal dynamical ejecta configurations from binary neutron star merger simulations (Rosswog et al. 2014) and a sequence of spherically symmetric ejecta configurations from an analytic hydrodynamical model.

The composition of the NSM outflow determines both the nuclear heating rates, which power the macronova, and the opacity of the ejecta. In our models, the nuclear heating rates are taken directly from the output of the r -process network WinNET (similar to Rosswog et al. 2017). Time-dependent detailed compositions of decaying isotopes allow accurate calculation of nuclear energy partitioning between different decay products (α -, β -, γ - radiation and fission products). We then apply analytic fits from Barnes et al. (2016) to compute energy thermalization for each of the decay products. For the γ -ray thermalization efficiency, in multiple dimensions, we either ray-trace from the origin to obtain optical depths or perform Monte Carlo. In either case, we use a grey, pure-absorption γ -ray opacity, calibrated to accurately reproduce energy deposition from Compton scattering and photoionization (see Fig.5 in Barnes et al. 2016).

Our opacity treatment is limited to detailed multifrequency opacities for a few selected representative elements, with an assumption of local thermodynamic equilibrium (LTE opacities). The opacities are calculated with the Los Alamos suite of atomic physics codes (Fontes et al. 2015b). The elements are selected either due to their higher abundance in dynamical ejecta or wind, or due to an open f -shell in their atomic structure. We also explore simple density-weighted mixtures of representative elements.

Because of heavy line blanketing in lanthanides, and even actinides, (Mendoza-Temis et al. 2015) abundantly present in the dynamical ejecta (Rosswog et al. 2017, find mass fractions $> 20\%$), the detection of electromagnetic counterparts directly from the heavy r -process ejecta is very difficult. However, if the distribution of lanthanides has a quasi-toroidal morphology due to preferentially equatorial ejection or neutrino irradiation in polar regions (Wanajo et al. 2014), there is a possibility of detecting an additional blue component from the lanthanide-free "polar caps". In this study, we consider a range of configurations of dynamical ejecta and wind outflows, and investigate the "opening angle" of visibility for these configurations in optical bands.

The uncertainties and interdependencies of the morphology, composition, opacity, and nuclear heating in NSM outflow make characterizing the macronova signal a challenging problem. In this work, we attempt to isolate and examine the impact of each of these aspects on the macronova signal; we first summarize the methods and approximations for the simulations. Specifically, in Sect. 2.1, we describe the origin and hydrodynamics of various types of NSM outflows, give typical estimates of their parameters, and derive an analytic spherically-symmetric homologously expanding solution. In Sect. 2.2, we provide motivation for the composition and r -process heating rates that dictate the opacity and provide the power source for the luminosity. In Sect. 2.3, we discuss the radiative transfer and opacity methods employed to obtain light curves and spectra. Here we also discuss some past and current code verifications. In Sect. 3, we study various aspects of macronovae for a range of models with increasing level of sophistication, starting from simple spherically-symmetric models with grey opacity, and ending with complex combined 2D axisymmetric models with dynamical ejecta and wind, having detailed elemental opacities. In Sect. 4, we synthesize light curves and spectra for our most realistic models, which include mixed compositions for wind and dynamical ejecta and detailed r -process radioactive energy source. In Sect. 5 we assess

the detection prospects of our most realistic models using limiting magnitudes from VISTA and LSST. We consider these theoretical detection prospects in the context of recent estimates for macronova detection rates. Finally, in Sect. 6, we discuss and summarize our findings.

2 METHODOLOGY

2.1 Expansion dynamics

NSM outflows can be divided into two main classes: dynamical ejecta and "winds". The "winds" are assumed to be ejected by the sum of all other processes, such as powerful neutrino emission, viscous and magnetic stresses, and energy which is released in the post-merger accretion disk due to nuclear recombination (Dessart et al. 2009; Perego et al. 2014; Martin et al. 2015; Chen & Beloborodov 2007; Siegel et al. 2014; Ciolfi & Siegel 2015; Metzger et al. 2008; Fernández & Metzger 2013; Just et al. 2015; Wu et al. 2016).

Dynamical ejecta have been studied extensively (Rosswog et al. 1999; Rosswog 2013; Bauswein et al. 2013; Hotokezaka et al. 2013; Sekiguchi et al. 2016; Lehner et al. 2016; Rosswog et al. 2017; Endrizzi et al. 2016), and the consensus on the value of total ejected mass is the range between 10^{-4} and $\sim 0.05 M_{\odot}$. These are also the ranges used in recent population synthesis and chemical evolution studies (Fryer et al. 2015; Côté et al. 2017). Eccentric binaries or parabolic encounters can unbind an order of magnitude more mass (Rosswog 2013; Gold et al. 2012; East et al. 2012; Radice et al. 2016), but such events are expected to be very rare. Mergers of neutron stars with black holes can release up to $0.2 M_{\odot}$ of material (Rosswog 2005; Foucart et al. 2015; Kyutoku et al. 2015; Kawaguchi et al. 2015; Foucart et al. 2016).

Dynamic ejecta become unbound at the moment of contact. They fall in two categories, "tidal ejecta" unbound by gravitational torques and "interaction ejecta" that become unbound due to hydrodynamic processes (see Fig.2 in Korobkin et al. (2012)). The first component is cold and extremely neutron-rich (with electron fractions $Y_e < 0.04$), while the second component can potentially have higher Y_e resulting from the copious production of e^-e^+ -pairs, which rapidly drives matter to a more symmetric state (Wanajo et al. 2014; Radice et al. 2016). Further irradiation of the rapidly receding dynamical ejecta by neutrinos from the surface of the hot transient hypermassive neutron star, however, does not alter its composition very much, because the ejecta are sufficiently far away when neutrino emission becomes significant (Radice et al. 2016; Foucart et al. 2015). Most recent studies agree that the combined electron fraction of the dynamical ejecta is in the range $Y_e \sim 0.04 - 0.25$, which allows for one or more nuclear fission cycles and a robust main r -process nucleosynthesis (Korobkin et al. 2012). As a consequence, dynamical ejecta will have high abundances of elements with an open f -shell – lanthanides and actinides (see Table 1 in Rosswog et al. 2017). The open f -shell of these elements furnish extremely high opacity in visible bands and lead to dimmer and slower evolving transients peaking in the infrared (Barnes & Kasen 2013; Kasen et al. 2015; Fontes et al. 2015a, 2017).

The morphology of the dynamical ejecta depends on the compactness of the merging stars and the binary mass ratio. Higher mass ratios produce more massive tidal ejecta (Rosswog 2013) which tend to have a toroidal shape (Rosswog et al. 2014), while softer equations of state and inclusion of general relativistic gravity enhances shocks which lead to more irregular and isotropic outflow

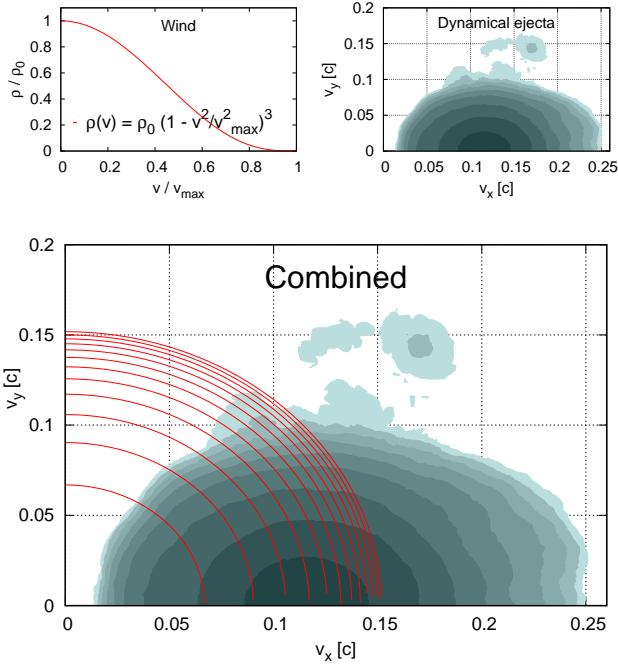


Figure 1. Density profiles, illustrating three types of morphology of the outflows explored in this study. Top left: radial density profile of the spherically-symmetric analytic models. Top right: axisymmetric averaged profile of dynamical ejecta from NSM simulations. Bottom: density profiles of combined models, with the wind and dynamical ejecta density and composition superimposed. Density contours of the two latter axisymmetric plots are in log space, separated by 0.25 dex.

shapes, dominated by the interaction component (Bauswein et al. 2013).

Increased interest due to the possibility of an additional, bluer component from secondary outflows has resulted in a number of recent wind studies (Dessart et al. 2009; Grossman et al. 2014; Perego et al. 2014; Martin et al. 2015; Metzger & Fernández 2014; Just et al. 2015; Fernández et al. 2015). The general consensus here is that the wind component has higher Y_e , which prevents formation of lanthanides. The morphology of the wind outflow is very sensitive to a variety of factors, but the studies converge on the fact that wind outflows are generally slower than the dynamical ejecta (0.01-0.15 c vs. \sim 0.1-0.3 c). The mass of the wind component is also highly uncertain – estimates vary from $10^{-4} M_\odot$ up to a few $10^{-1} M_\odot$, depending on the assumptions about the lifetime of the hypermassive neutron star (Perego et al. 2014) or mass of the accretion disk (Metzger & Fernández 2014). In asymmetric mergers the disk masses can easily reach several $0.1 M_\odot$ (Giacomazzo et al. 2013) and as much as 20 % of these masses can become unbound at late times (Fernández & Metzger 2013; Just et al. 2015).

The morphology of the outflow is crucial for the visibility of the blue transient. Here we explore three types of morphologies: spherically-symmetric analytic density profiles (Sect. 2.1.1), axisymmetric dynamical ejecta from NSM simulations (Sect. 2.1.2), and combined models where we superimpose the first two models (Sect. 2.1.3), as illustrated in Fig. 1. We explain the naming conventions of our models in Table 1 with more detailed parameters for each model listed in Table 3.

Table 1. Naming conventions for the models used in this paper.

	Notation	Comments
spherically symmetric analytic models	SA +	varying mass expansion velocity grey opacity
sph.-symmetric models with multigroup opacity	SA +	Se, Br, Te, Pd, Cr, Zr Sm, Ce, Nd, U d w1, w2
dynamical ejecta morphologies	A B C D	spherically (1d) or axisymmetrically (2d) averaged morphologies with opacity of Sm
axisymmetric (2d) ejecta + wind (W) models	W2 +	A, B, C, D Se, Br, Te, Pd, Cr, Zr light/heavy slow/fast
detailed composition and nuclear heating		opacity mixtures for dynamical ejecta + two types of wind enhanced heating rates Xnh1, Xnh2
most realistic models		$\gamma A_1, \gamma B_1, \gamma C_1, \gamma D_1,$ $\gamma A_2, \gamma B_2, \gamma C_2, \gamma D_2$ Xnh1, Xnh2 + γ -transfer + morphologies A-D

2.1.1 Analytic models in spherical symmetry

Consider a spherically-symmetric outflow expanding in vacuum. The motion of the fluid can be described by the Euler equations of ideal hydrodynamics in spherical coordinates:

$$\frac{\partial \rho}{\partial t} + \frac{\partial}{\partial r}(\rho v) = -\frac{2}{r} \rho v, \quad (1)$$

$$\frac{\partial v}{\partial t} + v \frac{\partial v}{\partial r} + \frac{1}{\rho} \frac{\partial p}{\partial r} = 0, \quad (2)$$

where v is the radial velocity, ρ and p are density and pressure, and r and t are the radial coordinate and time. These equations represent conservation of mass and momentum, and if the flow is adiabatic then the conservation of energy follows. For a self-similar homologous solution there exist functions $R(t)$ (scale parameter) and $\varphi(x)$ (shape function with the dimensionless radius coordinate $x = r/R(t)$) such that the density and the velocity can be expressed as:

$$\rho(t, r) = R(t)^{-3} \varphi(r/R(t)), \quad (3)$$

$$v(t, r) = r \dot{R}(t)/R(t). \quad (4)$$

This ansatz automatically satisfies the continuity equation. The momentum conservation equation becomes:

$$r \frac{\ddot{R}}{R} + \frac{1}{\rho} \frac{\partial p}{\partial \rho} R^{-4} \varphi' = 0, \quad (5)$$

(where the prime superscript and over-dot indicate the derivative with respect to x and t , respectively). Using a polytropic equation of state above, the momentum equation can be rewritten as a sum with one term containing the time dependence while the other depends on the dimensionless radius x :

$$\ddot{R} R^{3\Gamma-2} + K \Gamma \varphi^{\Gamma-2} \varphi' \cdot \frac{1}{x} = 0. \quad (6)$$

But this is only possible if both terms are constant:

$$\ddot{R} R^{3\Gamma-2} = -K \Gamma \varphi^{\Gamma-2} \varphi' / x = C. \quad (7)$$

Both ODEs admit closed-form solutions for special choices of Γ . For radiation-dominated flows with $\Gamma = 4/3$ it is convenient to

express the solution in the following closed form:

$$\varphi(x) = \rho_0 R_0^3 (1 - x^2)^3, \quad (8)$$

$$(t - t_0) = \frac{R(t)}{V} \sqrt{1 - \frac{R_0}{R(t)}} + \frac{R_0}{V} \log \left[\frac{R(t)}{R_0} \left(1 - \sqrt{1 - \frac{R_0}{R(t)}} \right)^2 \right], \quad (9)$$

where R_0 is the initial characteristic radius of the outflow, ρ_0 is the initial central density, and V is the expansion velocity.

Notice that for $t \gg t_0$ equation (9) reduces to a trivial linear dependence: $R(t) \approx Vt$. Because the condition $t \gg t_0$ is certainly valid during the time when electromagnetic signals are expected, we can safely ignore any nonlinearity in (9) and arrive at the following expansion profile:

$$\rho(t, r) = \rho_0 \left(\frac{t}{t_0} \right)^{-3} \left(1 - \frac{r^2}{v_{\max}^2 t^2} \right)^3. \quad (10)$$

Here, ρ_0 is initial central density at time t_0 and v_{\max} is the velocity of the expansion front (see Fig. 1, top left panel for an illustration). These parameters can be easily related to the total mass m_{ej} and average velocity \bar{v} of the outflow:

$$m_{\text{ej}} = 4\pi \rho_0 t_0^3 v_{\max}^3 \int_0^1 (1 - x^2)^3 x^2 dx = \frac{64\pi}{315} \rho_0 t_0^3 v_{\max}^3, \quad (11)$$

$$\bar{v} = \frac{1}{m_{\text{ej}}} \int 4\pi r^2 \rho(r) v dr = \frac{63}{128} v_{\max} \approx \frac{1}{2} v_{\max}. \quad (12)$$

The analytic solution is based on the assumptions that: (a) the internal energy of the outflow is negligible compared to its kinetic energy; and (b) the outflow is radiation-dominated and thus can be described by a polytropic equation of state $p = K\rho^\Gamma$ with $\Gamma = 4/3$. For dynamical ejecta, these assumptions have been shown to be accurately fulfilled (Rosswog et al. 2014). Although the second assumption breaks down at later times when radiation can freely escape, by then it has already established a homologous expansion pattern, with shells at different radii being out of sonic contact. Finally, we adopt a non-relativistic approach, consistent with the expansion velocities $\ll c$ (but note that our radiative transfer solver SuperNu takes into account relativistic corrections up to $O(v/c)$ in the treatment of Monte Carlo photon particles; see Sect. 2.3).

An ideal gas equation of state also suggests the following profile for the radial shape of the temperature:

$$T(r, t) = T_0 \left(\frac{\rho(r, t)}{\rho_0} \right)^{1/3} = T_0 \left(\frac{t}{t_0} \right)^{-1} \cdot \left(1 - \frac{r^2}{v_{\max}^2 t^2} \right). \quad (13)$$

Here, T_0 is the temperature at the center at initial time $t = t_0$. However, the temperature is much more sensitive to the details of the equation of state and interaction between matter and radiation and nuclear energy input, so this temperature dependence has to be regarded only as a very simple estimate. In our radiative transfer simulations, the temperature is recomputed inside SuperNu based on detailed composition, radiative losses and local energy input from the radioactive source (see Sect. 2.3). Consequently, we only use equation (13) to initialize our radiative transfer simulations.

2.1.2 Dynamical ejecta models

Spherically-symmetric models are often used as an approximation for isotropic dynamical ejecta or for the case when the dynamical ejecta completely obscure the blue transient from the wind. To verify

this approximation and test the impact of ejecta asphericity on the light curves, we explore axisymmetric dynamical ejecta based on morphologies from Rosswog et al. (2014) (the same as used in Kasen et al. 2015; Fontes et al. 2015a, 2017). The latter were computed by long-term hydrodynamic evolution (up to 100 years after the merger) with radioactive heating source (Rosswog et al. 2014), following simulations of NSMs (Rosswog 2013). NSM simulations were performed with the smoothed particle hydrodynamics (SPH) method in Newtonian gravity (Rosswog et al. 2000; Rosswog 2005; Rosswog & Price 2007; Rosswog 2015a), with a nuclear equation of state (Shen et al. 1998b,a) and an opacity-dependent multiflavour neutrino leakage scheme (Rosswog & Liebendörfer 2003) to take care of the changes in the neutron to proton ratio and the cooling by neutrino emission.

Relevant parameters of the models of dynamical ejecta are given in Table 5 and notation (A–D) is the same as in Rosswog et al. (2014) and Grossman et al. (2014). For each of these four 3D morphologies we compute three different effective 1D and 2D density distributions, distinguished by three different types of averaging. Models A1dSm–D1dSm are computed by spherical averaging of the density:

$$\rho(r) = \frac{1}{4\pi} \int_{4\pi} \rho(r, \theta, \varphi) d\Omega. \quad (14)$$

Models A2dSm–D2dSm are computed by azimuthal averaging:

$$\rho(R, z) = \frac{1}{2\pi} \int_0^{2\pi} \rho(R, z, \varphi) d\varphi. \quad (15)$$

Finally, in models A1dmSm–D1dmSm the abbreviation "m" stands for "density maximum": we first find the radius R_{\max} of the circle at which the density in the equatorial plane reaches its maximum, and then average the density distribution with respect to the distance to that circle:

$$\rho(\xi) = \frac{1}{4\pi^2} \int_0^{2\pi} \int_0^{2\pi} \rho(\xi, \alpha, \varphi) d\alpha d\varphi. \quad (16)$$

Here $\{\xi, \alpha, \varphi\}$ are toroidal coordinates around the circle of maximal density. This type of averaging is designed to test how much the light curve is affected by the optical depth of the emitting layer versus geometry of the outflow.

Figure 2 displays the resulting azimuthally and spherically averaged density distributions. Since we assume a simple homologous expansion that is attained within about one hour after the merger (as demonstrated in Rosswog et al. 2014), the density profiles are shown in velocity space. Given the initial density profile $\rho_0(\mathbf{v})$ at time t_0 , dynamical ejecta density at a later time t at a point \mathbf{r} is calculated as:

$$\rho(t, \mathbf{r}) = \left(\frac{t}{t_0} \right)^{-3} \rho_0 \left(\frac{\mathbf{r}}{t} \right). \quad (17)$$

Figure 2 (bottom panel, thin dashed line), shows a fit of the analytic density profile of type described by Eq.(10) in comparison to a spherically averaged numerical density profile. It agrees with the density profile for model A for large velocities and deviates from it significantly near the origin where model A has a hole.

2.1.3 Combined models of dynamical ejecta and wind

In combined models of dynamical ejecta and wind, we take axisymmetric models of the dynamical ejecta and amend them with various parameterized spherically-symmetric density distributions for the wind, as illustrated in Fig. 1 (bottom panel). Because morphology, mass and composition of the wind are rather uncertain, we explore

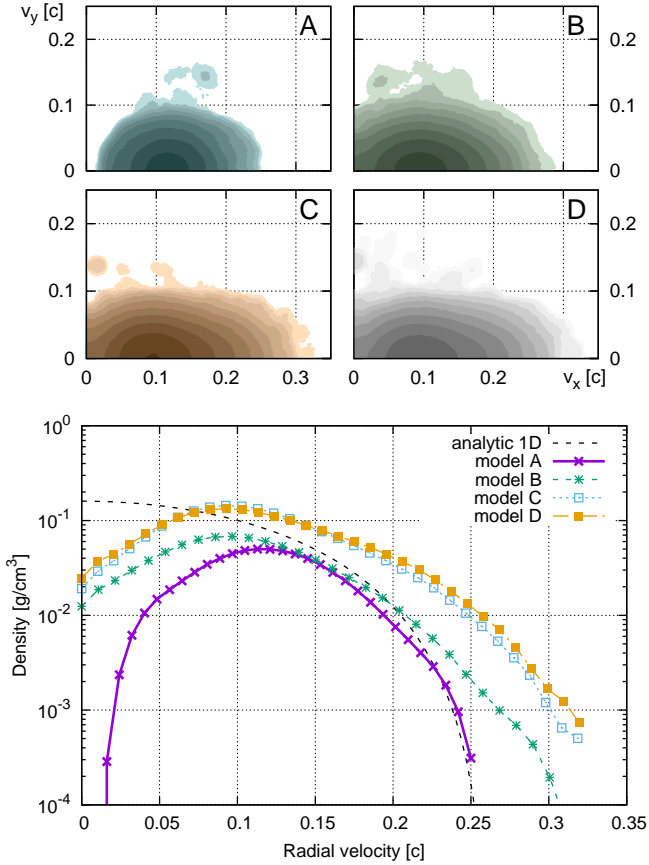


Figure 2. Morphology of the dynamical ejecta models A-D from binary neutron star merger simulations, plotted in velocity space. Top: azimuthally averaged density; the contours are in log space, separated by 0.25 dex. Bottom: spherically averaged density profiles. Thin dashed line represents an analytic fit with $v_{\max} = 0.3 c$, $m_{\text{ej}} = 0.013 M_{\odot}$.

a range of parameters listed in Table 6. The added density profile for the wind is modelled with the analytic spherically-symmetric distribution (10). When combining two outflows, we simply add the corresponding densities and weighted compositions at every point and ignore potential hydrodynamical interaction between the wind and dynamical ejecta. This is certainly a strong simplification, we leave the exploration of this hydrodynamic interaction to future work.

2.2 Matter composition

We compute the compositional evolution within the ejecta with the network code WinNET (Winteler 2012; Winteler et al. 2012) that is derived from the BasNet network (Thielemann et al. 2011). The network includes 5831 isotopes reaching up to $Z = 111$ between the neutron drip line and stability. The reaction rates are from the compilation of Rauscher & Thielemann (2000) for the finite range droplet model (FRDM; Möller et al. 1995) and the weak interaction rates ($e^- e^+$ -captures and β -decays) are the same as used in Arcones & Martínez-Pinedo (2011). For fission and neutron capture, we use fission rates of Panov et al. (2010) and β -delayed fission probabilities as described in Panov et al. (2005).

We use FRDM as our baseline model, but it needs to be stressed that the nuclear heating rates for ejecta that contain matter beyond

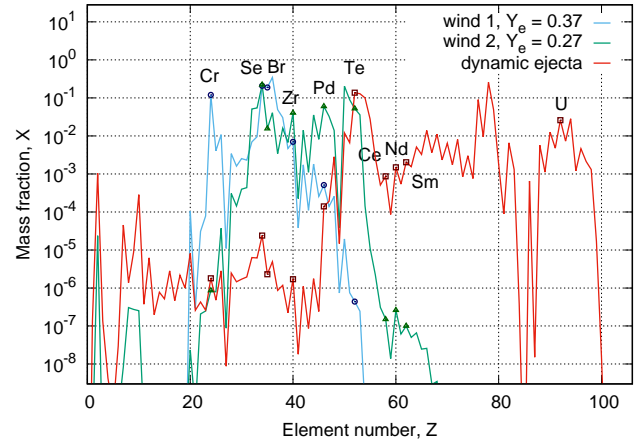


Figure 3. Mass fractions of the elements in different parts of the wind and in the ejecta, as a function of atomic number Z .

the platinum peak is strongly impacted by the used mass formula, see Barnes et al. (2016) and Rosswog et al. (2017). From the four mass formulae explored by Barnes et al. (2016), FRDM yielded the smallest and Duflo-Zucker (DZ) the largest nuclear heating rates. At the times most relevant for macronovae, the heating from DZ can be an order of magnitude larger than the one from FRDM, see Fig. 7, left panel, in Rosswog et al. (2017).

Dynamical ejecta composition and nuclear heating is approximated using a single particle trajectory from model B in Rosswog et al. (2014), and two representative tracers from previous studies on neutrino-driven winds: tracers H1 and H5 from Perego et al. (2014). A single trajectory from dynamical ejecta may be sufficient to represent nuclear heating, since the heating contribution is relatively robust (Metzger et al. 2010; Goriely et al. 2011; Lippuner & Roberts 2015), as is the final nucleosynthetic pattern (Korobkin et al. 2012; Lippuner & Roberts 2015).

For the wind, we pick two representative tracers with initial electron fractions $Y_e = 0.37$ and $Y_e = 0.27$. Fig. 3 displays the computed composition of dynamical ejecta and wind tracers for $t = 1$ day. Tracer H5 from Perego et al. (2014) is our "wind 1" model, it has a peak in abundances around iron group elements and around r -process first peak (Br). The other tracer, H1, is the "wind 2" model, and it produces the r -process pattern between first (Br) and second (Xe) peaks. Broader ranges of potential nucleosynthetic paths will be explored elsewhere.

For radiative transfer, a few representative elements are mixed in the same proportion as the one encountered in the composition of each type of outflow (dynamical ejecta, wind 1 and wind 2). Fig. 3 marks the mass fractions of the elements that we picked for detailed opacity calculation, and Table 2 lists their numerical values in each of the model outflows. These mass fractions are then used to mix approximate opacities in the mixed-composition models X1, X2 and all γ -models (see Table 6 and Sect. 3.4 for details on these models). As can be seen from the plot, winds contain a negligible fraction of elements with open f -shell (lanthanides or actinides), and as such are expected to be more transparent. Notice that the "wind 2" composition additionally contains very little elements with open d -shell. This makes "wind 2" more transparent than "wind 1", which is polluted by iron-group elements.

We first explore nuclear heating in the ejecta with the analytic power

Table 2. Mass fractions of representative elements in the two types of wind outflow and in the dynamical ejecta.

Elem.	Wind 1	Wind 2	Dynamical ejecta
²⁴ Cr	0.120	8.6×10^{-7}	1.8×10^{-6}
³⁴ Se	0.208	0.222	2.4×10^{-5}
³⁵ Br	0.188	0.0156	2.3×10^{-6}
⁴⁰ Zr	0.007	0.0405	1.7×10^{-6}
⁴⁶ Pd	5.1×10^{-4}	0.0598	1.4×10^{-4}
⁵² Te	4.4×10^{-7}	0.0523	0.137
⁵⁸ Ce	$< 10^{-20}$	1.5×10^{-7}	0.00087
⁶⁰ Nd	$< 10^{-20}$	2.6×10^{-7}	0.00149
⁶² Sm	$< 10^{-20}$	1.0×10^{-7}	0.00203
⁹² U	$< 10^{-20}$	$< 10^{-20}$	0.026

law fit (cf. Korobkin et al. 2012):

$$\dot{\epsilon}(t) = \epsilon_{\text{th}} \cdot 2 \times 10^{10} t_d^{-1.3} \text{ erg g}^{-1} \text{ s}^{-1}, \quad (18)$$

where t_d is time in days and ϵ_{th} is a fraction of energy that is left for thermalization (after all neutrinos and a certain fraction of gammas escaped). This fraction is normally taken to be $\epsilon \sim 0.2 - 0.5$; see Metzger et al. (2010) for details. We adopt a value of $\epsilon = 0.25$ in our models.

Models DZ₁ and DZ₂ explore the impact of increased nuclear heating. The rates of nuclear heating depend on the properties of the nuclei at the r -process path, which are currently unknown experimentally and highly uncertain theoretically. In particular, compared to other nuclear mass models, the FRDM nuclear mass model adopted in this work tends to underestimate heating rates for the time scales of macronovae (as demonstrated in Wu et al. 2016). Fig. 7 in Rosswog et al. (2017) shows one order of magnitude higher heating rates for the Duflou-Zucker DZ31 nuclear mass model (Duflou & Zucker 1995), computed with the network of Mendoza-Temis et al. (2015). In models DZ₁ and DZ₂, we use the expression (18) for heating, but increase the heating rate in the dynamical ejecta by a factor of 10. Otherwise, these models are identical to X₁ and X₂.

For our advanced models X1nh, X2nh and for all γ -models (as listed in Table 6) we use instead detailed time-dependent nuclear heating output from nucleosynthesis network which distinguishes different radiation species. The top panel of Fig. 4 shows the evolution of the fractions of nuclear heating rates which are carried away by different species, as computed by WinNET, and the bottom panel demonstrates total heating rates (without neutrinos), normalized to the energy generation given in Eq. (18) for comparison. Following the methodology developed by Barnes et al. (2016), we apply pointwise density-dependent analytic prescription for thermalization efficiencies in the wind and in the dynamical ejecta.

For a particle species " i " (α -, β - or fission fragments), the thermalization efficiency is calculated as follows:

$$f_i(t, \mathbf{r}) = \frac{\log(1 + 2\eta_i^2)}{2\eta_i^2}, \quad (19)$$

where the coordinate- and time-dependent quantity $2\eta_i^2$ (c.f. Rosswog et al. 2017) is defined as:

$$2\eta_i^2(t, \mathbf{r}) = \frac{2A_i}{t\rho(t, \mathbf{r})}, \quad (20)$$

and the constants A_i determine thermalization times: $\{A_\alpha, A_\beta, A_{\text{f}}\} = \{1.2, 1.3, 0.2\} \times 10^{-11} \text{ g cm}^{-3} \text{ s}$. These constants correspond to the choice of average particle energies $E_{\alpha,0} = 6 \text{ MeV}$, $E_{\beta,0} = 0.5 \text{ MeV}$, $E_{\text{f},0} = 100 \text{ MeV}$, and the same values of energy-loss rates for different species as originally computed in Barnes et al. (2016) (cf. their Eqs. 19 and 25).

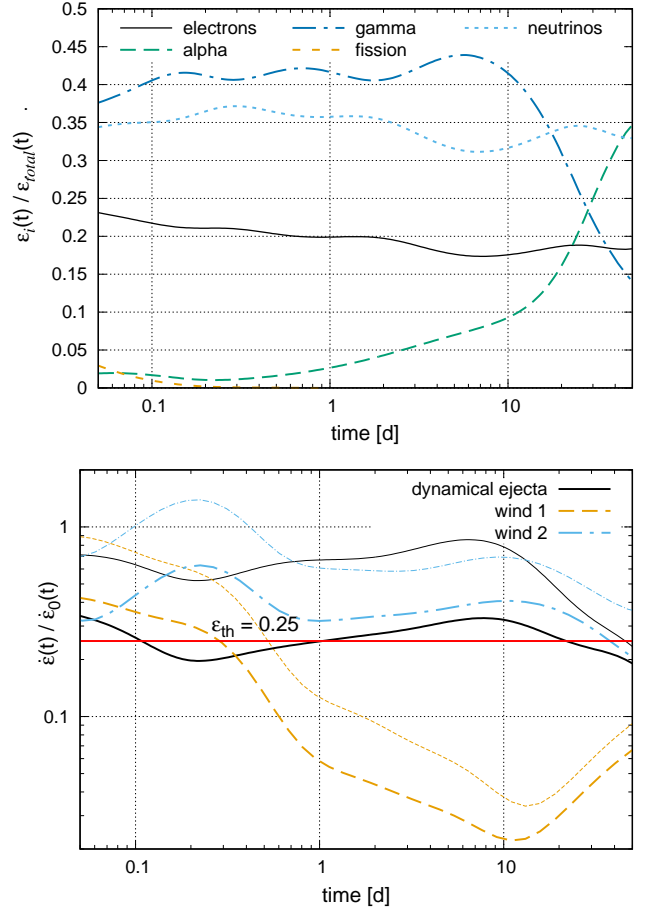


Figure 4. Top: partitioning of nuclear energy release between different radioactive species, as a function of time, calculated by WinNET for dynamical ejecta outflow. Bottom: peculiarities of the nuclear heating with (thin lines) and without (thick lines) contribution of γ -radiation, in dynamical ejecta and two different models of wind. Here, neutrinos are excluded, and the heating rates are normalized to the analytic power law (18). The rate with $\epsilon_{\text{th}} = 0.25$ used in simpler models is also shown for reference.

In models X1nh and X2nh we adopt coordinate-dependent thermalization for γ -particles as well. Specifically, we use a thermalization efficiency of $f_\gamma = 1 - e^{-\tau}$, where

$$\tau(t, r) = \int_{vt}^{v_{\text{max}}t} \kappa_\gamma \rho(t, r) dr, \quad (21)$$

and κ_γ is an average opacity in the γ -ray band. Instead of adopting an approximate expression for τ , we calculate the radial optical depth directly from our ejecta morphology and spatial grid, assuming density is piecewise constant over the spatial cells. The piecewise-constant treatment for density in the calculation of τ is consistent with the treatment of opacity and energy deposition for Monte Carlo. For all models with detailed r -process heating, we use a grey γ -ray opacity value of $\kappa_\gamma = 0.1 \text{ cm}^2 \text{ g}^{-1}$ (same as used in Barnes et al. 2016).

Total nuclear input at a position \mathbf{r} and time t is calculated as a weighted average:

$$\dot{\epsilon}(t, \mathbf{r}) = \frac{\rho_{\text{wind}}(t, \mathbf{r})\dot{\epsilon}_{\text{wind}}(t, \mathbf{r}) + \rho_{\text{dyn}}(t, \mathbf{r})\dot{\epsilon}_{\text{dyn}}(t, \mathbf{r})}{\rho_{\text{wind}}(t, \mathbf{r}) + \rho_{\text{dyn}}(t, \mathbf{r})}, \quad (22)$$

where heating contributions from the wind (model 1 or 2) and

dynamical ejecta are calculated separately according to the detailed nucleosynthesis and composition in each of the components:

$$\dot{\epsilon}_{\text{wind}} = \sum_i f_i^{\text{wind}}(t, \mathbf{r}) \dot{\epsilon}_i^{\text{wind}}, \quad \dot{\epsilon}_{\text{dyn}} = \sum_j f_j^{\text{dyn}}(t, \mathbf{r}) \dot{\epsilon}_j^{\text{dyn}}. \quad (23)$$

Subscripts i and j indicate the radioactive species. The sums give the total heating rate available for local heating in a parcel of the wind or dynamical ejecta (Barnes et al. 2016; Rosswog et al. 2017). In taking the average weighted by partial density of the sums, we are assuming the dynamical ejecta and winds are uniformly mixed in the spatial cells where they overlap.

2.3 Radiative transfer and opacity

We compute our light curves and spectra with the radiative transfer software SuperNu (Wollaeger & van Rossum 2014), with opacity from the state-of-the-art Los Alamos suite of atomic physics codes (Fontes et al. 2015a,b). Here, we describe some aspects of the radiative transfer and opacity that make them viable for macronova simulations.

2.3.1 Radiative transfer

SuperNu is a multidimensional Monte Carlo radiative transfer code specialized for synthesizing light curves and spectra of supernovae (see Wollaeger & van Rossum 2014; Wollaeger et al. 2013; van Rossum et al. 2016). More generally, the code is designed for modeling thermal radiative transfer in expanding, partially ionized plasma with radioactive sources (Wollaeger & van Rossum 2014). SuperNu has an implementation of Implicit Monte Carlo (IMC) and Discrete Diffusion Monte Carlo (DDMC); DDMC accelerates simulations with optically thick regions (see Fleck & Cummings 1971; Densmore et al. 2007, 2012; Abdikamalov et al. 2012). The Monte Carlo particles are tracked through a velocity grid, which relates to the spatial grid through the homologous approximation (Kasen et al. 2006),

$$\vec{v} = \frac{\vec{r}}{t}, \quad (24)$$

where \vec{v} , \vec{r} , and t are the velocity, radial coordinate and time. Relativistic corrections are accounted for in the radiative transfer to order $O(v/c)$, and the effect of the radiation on the ejecta momentum is assumed to be negligible. These are often reasonable approximations for supernovae and macronovae (see Kasen et al. 2006; Barnes & Kasen 2013).

The resulting tally of energy absorbed by the ejecta is used to update the temperature in each spatial cell, using the standard IMC approach (Fleck & Cummings 1971). The IMC equation for temperature is (Fleck & Cummings 1971; Wollaeger et al. 2013),

$$C_{v,n} \frac{DT}{Dt} = \mathcal{E} - f_n \sigma_{P,n} a c T_n^4 + f_n \rho_n \dot{\epsilon}, \quad (25)$$

where $C_{v,n}$, $\sigma_{P,n}$, T_n , and ρ_n are the heat capacity, Planck opacity, temperature, and density at time step n . The Fleck factor,

$$f_n = \frac{1}{1 + 4aT_n^3 \sigma_{P,n} c \Delta t_n / C_{v,n}}, \quad (26)$$

is a result of semi-implicitly discretizing the temperature (or internal energy) equation in time (Fleck & Cummings 1971). The value of \mathcal{E} is the rate of energy effectively absorbed in the comoving frame during time step n , per unit volume. Approximations made to obtain equation (25) are consistent with those typically made for radiative

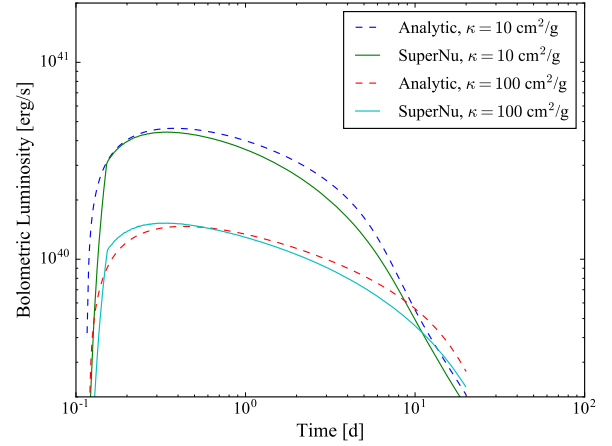


Figure 5. Bolometric light curves for a simple macronova-type spherical outflow from SuperNu and an analytic model.

transfer in supernovae (see Kasen et al. 2006), and are also valid for macronovae (Barnes & Kasen 2013; Kasen et al. 2013; Hotokezaka et al. 2013).

We supply a simple analytic verification here to ensure the radiative transfer produces accurate luminosities for macronova-type problems. The test problem has a uniform density with a total mass of $0.01 M_{\odot}$, a maximum outflow speed of $0.25c$, and a uniform grey absorption opacity of either 10 or $100 \text{ cm}^2 \text{ g}^{-1}$. The r-process heating rate is the analytic model in equation (18), with $\epsilon_{\text{th}} = 0.25$. The problem is started at 10000 seconds, with an initial uniform temperature of $1.5 \times 10^4 \text{ K}$. To derive the luminosity benchmark, we employ the normalizations and Fourier series expansion technique described by Pinto & Eastman (2000). For this problem, Fig. 5 has bolometric light curves from the analytic model and SuperNu. The analytic solution is of the equilibrium comoving radiation diffusion equation with a simple outer-boundary condition. Further details of this solution can be found in the Appendix A.

Apart from analytic radiative transfer solutions (Wollaeger et al. 2013; Wollaeger & van Rossum 2014), SuperNu has been tested against other supernova light curve codes. Benchmarks include the deterministic code PHOENIX (van Rossum 2012) for the W7 model of Type Ia supernovae (SN Ia) (Wollaeger & van Rossum 2014), and the codes STELLA (Blinnikov et al. 2006), RHMC (Noebauer et al. 2012), and V1D (Livne 1993) for a grey pair-instability supernova model (Kozyreva et al. 2017). For the SN Ia W7 comparison with the PHOENIX code, the peak bolometric luminosities differ by $\sim 10 - 15 \%$ (with subsequent more controlled comparisons bringing this to $\sim 5 - 10 \%$), and very close spectral profiles (see Figs. 7 and 8 of Wollaeger & van Rossum 2014). Similarly close agreement was found with the other codes for the grey pair-instability supernova model (see Fig. 9 of Kozyreva et al. 2017). For a double-degenerate white dwarf merger model, light curves and spectra from SuperNu have been compared to observations of the slowly declining SN Ia, SN 2001ay, producing similar broadband magnitudes and spectra (see Figs. 8 and 12 of van Rossum et al. 2016).

For realistic opacities, SuperNu calculates bound-bound contributions with line lists, and tabulated data for bound-free and free-free contributions (Verner et al. 1996; Sutherland 1998). These contributions are added into a 100-1000 group wavelength grid, which is defined in the ejecta's comoving frame, typically spanning UV (.01

μm) to IR ($3.2 \mu\text{m}$) for supernovae (Wollaeger & van Rossum 2014). Lines are treated like Dirac delta functions when they are grouped, so they each only contribute to one group. This also spreads the contribution of the line over the group. During the transport phase, Monte Carlo particles sample collision distances from only the resulting grouped opacity structure. Thus, unlike the typical Sobolev expansion opacity formalism in Monte Carlo codes (see, for instance, Kasen et al. (2006); Kromer & Sim (2009)), line transfer is not directly treated by SuperNu.

2.3.2 Opacity

We use the Los Alamos suite of atomic physics codes (Fontes et al. 2015b) to calculate the detailed multifrequency LTE opacities for the few representative elements listed in Table 2. The elements are selected to represent the variety of compositions in the dynamical ejecta and in different types of winds (see Fig. 3): Lanthanides (Sm, Ce, Nd), an Actinide (U), lighter wind (Cr, Se, Br) and heavier wind (Zr, Pd, Te). The opacities are calculated on a 27-point temperature grid $0.01 \text{ eV} \leq k_B T \leq 5 \text{ eV}$ for density values sampled for every decade from $\rho_{\text{min}} = 10^{-20} \text{ g cm}^{-3}$ to $\rho_{\text{max}} = 10^{-4} \text{ g cm}^{-3}$. These temperature and density ranges suffice to cover the typical thermodynamic conditions encountered in expanding dynamical ejecta around the epoch when macronovae peak.

Figure 6 illustrates typical opacity profiles for a number of representative elements for plasma density $\rho = 10^{-13} \text{ g cm}^{-3}$ and temperature $T = 0.5 \text{ eV}$. As can be seen in the lower panel of Fig. 6, the opacities contain an artificial window from $\sim 0.06 - 0.17 \mu\text{m}$, due to the limited choice of transitions that were included in the atomic physics model in that range. For some of our simulations, this window in the opacity causes artificially enhanced emission in that wavelength range.

In our simulations, we do not apply the expansion opacity formalism (Karp et al. 1977; Eastman & Pinto 1993), which employs the Sobolev approximation (Sobolev 1960) and is adopted in previous detailed macronova radiative transfer calculations (Barnes & Kasen 2013; Kasen et al. 2013; Tanaka & Hotokezaka 2013). The method for calculating the opacities employed in this work has been previously described by Fontes et al. (2015a, 2017). Briefly, the lines are broadened using an effective Doppler width in the Voigt profile by $\Delta\lambda/\lambda \sim \Delta v/c \sim 0.01$. For the deterministic calculations of Fontes et al. (2017), this approach is used to take into account the shifting of lines due to the velocity gradients in the dynamical ejecta. The same approach is used here for both the wind and the dynamical ejecta as their velocity gradients are similar for all the models we simulate. This approach preserves the integral of the wavelength-dependent opacities, which can generate significantly larger values than those produced via the expansion opacity formalism. A practical advantage of this line-smearing approach is that the wavelength-dependent opacities can be represented with a reasonable number of photon energy points, making possible the generation of opacity tables that can be used in an efficient look-up approach in radiation transport simulations.

Of relevance for the application of the line-smearing opacities in SuperNu is the extent of line smearing relative to the group sizes in the wavelength grid. The group structure used in the radiative transfer step is logarithmic, with $\Delta\lambda/\lambda \sim 0.05$ for each group. Consequently, our group structure does not resolve the smeared lines. The groups, however, should resolve P-Cygni features that may appear in the spectra (these arise from the separation of line absorption and emission features in the spectra due to the velocity of the ejecta). For instance, at day 5 of the expansion for the density

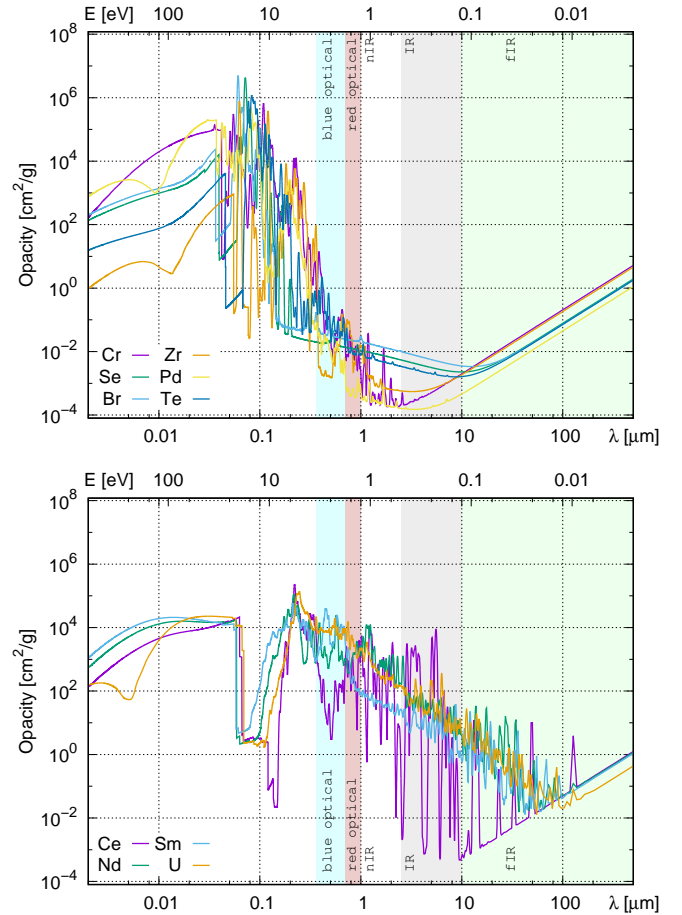


Figure 6. Profiles of opacity for pure elemental plasma at LTE for temperature $T = 5800 \text{ K}$ ($k_B T = 0.5 \text{ eV}$) and density $\rho = 10^{-13} \text{ g cm}^{-3}$. Top: elements representing the wind; bottom: heavy r -process lanthanides and actinides from dynamical ejecta. The dips in opacity around $0.1 \mu\text{m}$ are artificial, caused by the limited choice of transitions included in the atomic physics models.

profile in equation (10), $\kappa = 10 \text{ cm}^2/\text{g}$ gives a photosphere at about $v = 0.16c$. For a P-Cygni line feature at this photosphere, the span of wavelength between the emission feature and the absorption feature is $\Delta\lambda/\lambda = v_{\text{photo}}/c = 0.16$, where λ is the line center. This value of $\Delta\lambda/\lambda$ is a factor of ~ 3 larger than that of the multigroup grid, which in turn is a factor of ~ 5 larger than the effective broadening from the line smearing. These wavelength scales provide some justification for the use of line-smearing opacities and multigroup in the present simulations.

For some numerical justification, Fontes et al. (2017) compare light curves from SuperNu simulations of a pure-iron W7-type ejecta, using broadened LANL opacities, or SuperNu's default opacity calculation (see 2.3.1). For SuperNu's default opacity calculation, Fe lines were obtained from the Kurucz line list³. The light curves show a discrepancy of $\sim 20\%$ in the peak luminosities of broadband and bolometric light curves.

³ <http://kurucz.harvard.edu/atoms.html>

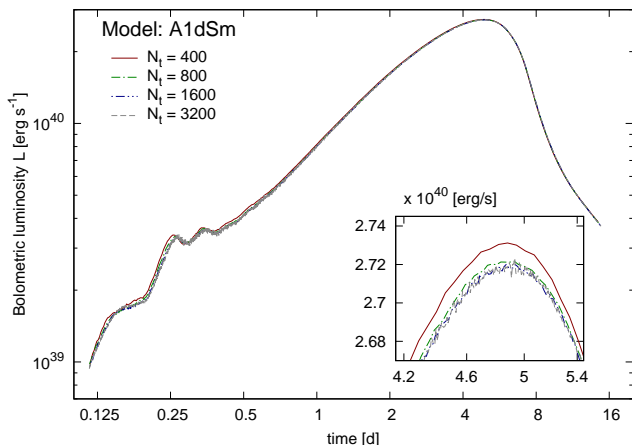


Figure 7. Bolometric light curves for four different time resolutions used in spherically-symmetric dynamical ejecta model A with LTE opacities of elemental Sm plasma (A1dSm, see Table 5). Number of timesteps covers 20 days in the comoving frame.

2.3.3 Time resolution test

With the opacity and radiative transfer methods in place, we performed several resolution tests. For instance, to properly select temporal numerical resolution, we tested the sensitivity of our results to timestep size on spherically-symmetric model of dynamical ejecta with LTE opacities of elemental Sm (see Table 5). Fig. 7 shows the bolometric luminosity for four different resolutions with progressively smaller timesteps, covering time period of 20 days with $N_t = 400, 800, 1600$ and 3200 timesteps. The number of photon wavelength groups ($N_\lambda = 100$) and the number of radial cells ($N_r = 128$) were kept constant. Under these conditions, the light curves show clear first-order convergent behavior, as expected from the numerical scheme. We have therefore selected the highest resolution $N_t = 3200$ per 20 days (in comoving frame) everywhere in this study.

3 SENSITIVITY STUDIES

We covered a range of models with progressively increasing levels of sophistication, gradually adding ingredients and observing their impact on the light curves and spectra. Model parameters are summarized in Table 3.

We start with simple models with wavelength-independent "grey" opacity and spherically-symmetric analytic density profiles (see Sect. 3.1). For nuclear heating, the analytic power law fitting formula (18) is adopted with thermalization efficiency $\epsilon_{\text{th}} = 0.25$. These models explore a range of masses (SAm1-SAm3), median expansion velocities (SAv1-SAv3) and grey opacities (SAk0-SAk2). We then explore the impact of composition (Sect. 3.2) by upgrading to multigroup opacity for single-element LTE plasmas, for ten representative elements (models SAsE - SAU). In all models with multigroup opacity, the opacity is binned into $N_\lambda = 100$ logarithmically spaced bins covering a wavelength range from $\lambda_{\text{min}} = 0.1$ to $\lambda_{\text{max}} = 12.8$ micron. Then, we use a simple mixing scheme to simulate multi-species composition models (introduced in Sect. 2.2) of dynamical ejecta (SAD) and two representative types of wind (SAw1 and SAw2).

Next, Section 3.3 describes models of just the dynamical

ejecta. Here we use different averaging for the dynamical ejecta simulations: spherically-symmetric (A1dSm-D1dSm), axisymmetric (A2dSm-D2dSm) and another set of spherically-symmetric models with a different type of averaging (A1dmSm-D1dmSm). In all these models, the same multigroup LTE opacities of Sm are employed to represent the lanthanides.

Combined models of the dynamical ejecta and wind are detailed in Sect. 3.4. W2A - W2D combine spherically-symmetric wind with different morphologies of dynamical ejecta to simulate the impact of a "lanthanide curtain" on potential blue transients from the wind. W2Se-W2Cr demonstrate variation in the macronova signature depending on the composition of the wind, while W2light/W2heavy and W2slow/W2fast explore sensitivity to the wind mass and velocity. The mixed multi-species composition of wind ("wind 1" and "wind 2", see Table 2) and dynamical ejecta are employed in models X1/X1.

In models X1nh and X2nh, macronova signals are calculated with upgraded detailed nuclear heating output and separate density-dependent thermalization efficiencies, as described in Sect. 2.2. In these models, a simple ray-trace is used with a calibrated grey opacity of $0.1 \text{ cm}^2 \text{ g}^{-1}$ to estimate the thermalization efficiency for γ -rays (Barnes et al. 2016). Finally, in the most sophisticated set of models, γA_1 - γD_2 , the γ -ray thermalization is replaced with energy deposition calculated from a grey, pure absorbing, Monte Carlo treatment (Swartz et al. 1995) (again using the calibrated grey opacity of Barnes et al. 2016).

3.1 Semianalytic models: grey opacity

The simplest models that we explore have grey opacity and spherically-symmetric analytic density distributions (described in Sect. 2.1.1). These models can be characterized by only three parameters: ejecta mass m_{ej} , grey opacity κ and expansion velocity v . We compare these models to the ones studied in Grossman et al. (2014). Parameters of these models are listed in Table 4. The baseline model (SAk1) implements dynamical ejecta mass and expansion velocity from simulations of a most typical neutron star binary with masses $1.4 M_\odot + 1.3 M_\odot$ (model B from Rosswog et al. 2014).

Figure 8 displays time evolution of bolometric luminosity for the four models with the range of grey opacities, SAK0 - SAK3 (thick lines), along with the light curves produced with a simple semi-analytic model from Grossman et al. (2014) (thin dotted lines on the plot). Triangle marks show locations of luminosity maxima for each of the models. As can be seen from the plot and more clearly in Fig. 10, the peak epochs t_p and peak luminosities L_p clearly follow a power law $L_p \propto t_p^{-1.7}$ with power index ≈ 1.7 that is close to the analytic result $\alpha = 1.3$ for the Grossman models. All calculations with full radiative transfer show an extended plateau with very small variation in luminosity, while the Grossman models instead exhibit a steeper rise and later peak times. Grossman models also underestimate bolometric luminosity, especially for high values of grey opacity, where the discrepancy exceeds one order of magnitude. This underestimate is likely related, in part, to the fact that the thermal contribution of the ejecta is completely neglected in the Grossman models.

The spectrum of grey opacity models turns out to be very close to Planck, as shown in Fig. 9 (top), where for each model SAK0 - SAK3 we plotted stacked spectra at different times (thin dashed lines), shifted and rescaled to match the Planck spectrum with the temperature at the peak epoch t_p . The temperature can be determined from the spectral peak location λ_{max} through the Wien law:

Table 3. Parameters of the models used in this study.

	Model	density profile wind + dyn. ejecta	$m_{\text{wind}}/m_{\text{ej}}$ [M_{\odot}]	$\bar{v}_{\text{wind}}/\bar{v}_{\text{ej}}^{\dagger}$ [c]	$\kappa_{\text{wind}}/\kappa_{\text{ej}}$ [$\text{cm}^2 \text{g}^{-1}$]	nuclear heating	thermali- zation	γ -ray treatment
Section 3.1: spherical symmetry, grey opacity	SAm1	1D analytic	0.001	0.125	10			–
	SAm2	1D analytic	0.01	0.125	10			–
	SAm3	1D analytic	0.1	0.125	10			–
	SAv1	1D analytic	0.014	0.05	10			–
	SAv2	1D analytic	0.014	0.10	10	power law	$\epsilon_{\text{th}} = 0.25$	–
	SAv3	1D analytic	0.014	0.15	10			–
	SAk0	1D analytic	0.014	0.125	1			–
	SAk1	1D analytic	0.014	0.125	10			–
	SAk2	1D analytic	0.014	0.125	100			–
SAk3	1D analytic	0.014	0.125	1000			–	
Section 3.2: spherical symmetry, multigroup opacity	SASe	1D analytic	0.014	0.125	κ_{Se}			–
	SABr	1D analytic	0.014	0.125	κ_{Br}			–
	SATe	1D analytic	0.014	0.125	κ_{Te}			–
	SAPd	1D analytic	0.014	0.125	κ_{Pd}			–
	SAZr	1D analytic	0.014	0.125	κ_{Zr}			–
	SACr	1D analytic	0.014	0.125	κ_{Cr}			–
	SACe	1D analytic	0.014	0.125	κ_{Ce}	power law	$\epsilon_{\text{th}} = 0.25$	–
	SASm	1D analytic	0.014	0.125	κ_{Sm}			–
	SANd	1D analytic	0.014	0.125	κ_{Nd}			–
	SAU	1D analytic	0.014	0.125	κ_{U}			–
	SAw1	1D analytic	0.014	0.125	κ_{wind1}			–
	SAw2	1D analytic	0.014	0.125	κ_{wind2}			–
SAd	1D analytic	0.014	0.125	κ_{dyn}			–	
Section 3.3: dyn. ejecta, spherical symmetry	A1dSm	1D spherically-averaged A	0.013	0.132	κ_{Sm}			–
	B1dSm	1D spherically-averaged B	0.014	0.125	κ_{Sm}			–
	C1dSm	1D spherically-averaged C	0.033	0.132	κ_{Sm}			–
	D1dSm	1D spherically-averaged D	0.034	0.136	κ_{Sm}	power law	$\epsilon_{\text{th}} = 0.25$	–
	A1dmSm	1D spherically-averaged A	0.013	0.066	κ_{Sm}			–
	B1dmSm	1D spherically-averaged B	0.014	0.080	κ_{Sm}			–
	C1dmSm	1D spherically-averaged C	0.033	0.055	κ_{Sm}			–
D1dmSm	1D spherically-averaged D	0.034	0.058	κ_{Sm}			–	
Section 3.3: axisymmetry	A2dSm	2D axisymmetric A	0.013	0.095	κ_{Sm}			–
	B2dSm	2D axisymmetric B	0.014	0.086	κ_{Sm}	power law	$\epsilon_{\text{th}} = 0.25$	–
	C2dSm	2D axisymmetric C	0.033	0.119	κ_{Sm}			–
	D2dSm	2D axisymmetric D	0.034	0.121	κ_{Sm}			–
Section 3.4: dyn. ejecta + wind	W2A (W2)	1D analytic + 2D axisym. A	0.005 + 0.013	0.08 + 0.095	$\kappa_{\text{Zr}} + \kappa_{\text{Sm}}$			–
	W2B	1D analytic + 2D axisym. B	0.005 + 0.014	0.08 + 0.086	$\kappa_{\text{Zr}} + \kappa_{\text{Sm}}$			–
	W2C	1D analytic + 2D axisym. C	0.005 + 0.033	0.08 + 0.119	$\kappa_{\text{Zr}} + \kappa_{\text{Sm}}$			–
	W2D	1D analytic + 2D axisym. D	0.005 + 0.034	0.08 + 0.121	$\kappa_{\text{Zr}} + \kappa_{\text{Sm}}$			–
	W2Se	1D analytic + 2D axisym. A	0.005 + 0.013	0.08 + 0.095	$\kappa_{\text{Se}} + \kappa_{\text{Sm}}$			–
	W2Br	1D analytic + 2D axisym. A	0.005 + 0.013	0.08 + 0.095	$\kappa_{\text{Br}} + \kappa_{\text{Sm}}$			–
	W2Te	1D analytic + 2D axisym. A	0.005 + 0.013	0.08 + 0.095	$\kappa_{\text{Te}} + \kappa_{\text{Sm}}$	power law	$\epsilon_{\text{th}} = 0.25$	–
	W2Pd	1D analytic + 2D axisym. A	0.005 + 0.013	0.08 + 0.095	$\kappa_{\text{Pd}} + \kappa_{\text{Sm}}$			–
	W2Zr (W2)	1D analytic + 2D axisym. A	0.005 + 0.013	0.08 + 0.095	$\kappa_{\text{Zr}} + \kappa_{\text{Sm}}$			–
	W2Cr	1D analytic + 2D axisym. A	0.005 + 0.013	0.08 + 0.095	$\kappa_{\text{Cr}} + \kappa_{\text{Sm}}$			–
	W2light	1D analytic + 2D axisym. A	0.001 + 0.013	0.08 + 0.095	$\kappa_{\text{Zr}} + \kappa_{\text{Sm}}$			–
	W2heavy	1D analytic + 2D axisym. A	0.02 + 0.013	0.08 + 0.095	$\kappa_{\text{Zr}} + \kappa_{\text{Sm}}$			–
	W2slow	1D analytic + 2D axisym. A	0.005 + 0.013	0.04 + 0.095	$\kappa_{\text{Zr}} + \kappa_{\text{Sm}}$			–
W2fast	1D analytic + 2D axisym. A	0.005 + 0.013	0.16 + 0.095	$\kappa_{\text{Zr}} + \kappa_{\text{Sm}}$			–	
Section 4: detailed composi- tion and nuclear heating	X ₁	1D analytic + 2D axisym. A	0.005 + 0.013	0.08 + 0.095	$\kappa_{\text{wind1}} + \kappa_{\text{dyn}}$	power law	$\epsilon_{\text{th}} = 0.25$	–
	X ₂	1D analytic + 2D axisym. A	0.005 + 0.013	0.08 + 0.095	$\kappa_{\text{wind2}} + \kappa_{\text{dyn}}$		$\epsilon_{\text{th}} = 0.25$	–
	DZ ₁	1D analytic + 2D axisym. A	0.005 + 0.013	0.08 + 0.095	$\kappa_{\text{wind1}} + \kappa_{\text{dyn}}$	$\times 10$	$\epsilon_{\text{th}} = 0.25$	–
	DZ ₂	1D analytic + 2D axisym. A	0.005 + 0.013	0.08 + 0.095	$\kappa_{\text{wind2}} + \kappa_{\text{dyn}}$	$\times 10$	$\epsilon_{\text{th}} = 0.25$	–
	Xnh ₁	1D analytic + 2D axisym. A	0.005 + 0.013	0.08 + 0.095	$\kappa_{\text{wind1}} + \kappa_{\text{dyn}}$	from network	species- dependent	–
	Xnh ₂	1D analytic + 2D axisym. A	0.005 + 0.013	0.08 + 0.095	$\kappa_{\text{wind2}} + \kappa_{\text{dyn}}$			–
Section 4: realistic models	γA_1	1D analytic + 2D axisym. A	0.005 + 0.013	0.08 + 0.095	$\kappa_{\text{wind1}} + \kappa_{\text{dyn}}$			grey
	γB_1	1D analytic + 2D axisym. B	0.005 + 0.014	0.08 + 0.086	$\kappa_{\text{wind1}} + \kappa_{\text{dyn}}$			grey
	γC_1	1D analytic + 2D axisym. C	0.005 + 0.033	0.08 + 0.119	$\kappa_{\text{wind1}} + \kappa_{\text{dyn}}$			grey
	γD_1	1D analytic + 2D axisym. D	0.005 + 0.034	0.08 + 0.121	$\kappa_{\text{wind1}} + \kappa_{\text{dyn}}$	from network	species- dependent	grey
	γA_2	1D analytic + 2D axisym. A	0.005 + 0.013	0.08 + 0.095	$\kappa_{\text{wind2}} + \kappa_{\text{dyn}}$			grey
	γB_2	1D analytic + 2D axisym. B	0.005 + 0.014	0.08 + 0.086	$\kappa_{\text{wind2}} + \kappa_{\text{dyn}}$			grey
	γC_2	1D analytic + 2D axisym. C	0.005 + 0.033	0.08 + 0.119	$\kappa_{\text{wind2}} + \kappa_{\text{dyn}}$			grey
γD_2	1D analytic + 2D axisym. D	0.005 + 0.034	0.08 + 0.121	$\kappa_{\text{wind2}} + \kappa_{\text{dyn}}$			grey	

(\dagger) For 1D analytic density profiles, $\bar{v} = v_{\text{max}}/2$, and for the numerical density distributions it is median velocity, namely such that half the mass moves faster, while the other half is slower than \bar{v} .
MNRAS **000**, 1–?? (2017)

Table 4. Summary of spherically-symmetric analytic (SA*) models. All models use a logarithmic time grid with $N_t = 1600$ time steps. Columns specify: total ejecta mass, half the maximum ejecta velocity $v_{\max}/2 \approx \bar{v}$ (see Eq. 12), opacity model, bolometric peak time, peak bolometric luminosity, and the effective blackbody temperature.

Model	m_{ej} [M_{\odot}]	$v_{\max}/2$ [c]	κ [$\frac{\text{cm}^2}{\text{g}}$]	t_p [d]	L_p [$\frac{10^{40} \text{erg}}{\text{s}}$]	$T_{\text{eff},p}$ [K]
SAm1	0.001	0.125	10	0.46	1.18	4092
SAm2	0.01	0.125	10	0.92	3.32	3724
SAm3	0.1	0.125	10	2.00	8.41	3173
SAv1	0.014	0.05	10	1.74	1.90	3668
SAv2	0.014	0.10	10	1.17	3.17	3622
SAv3	0.014	0.15	10	0.89	4.50	3730
SAk0	0.014	0.125	1	0.51	13.84	7233
SAk1	0.014	0.125	10	1.01	3.82	3728
SAk2	0.014	0.125	100	2.22	0.958	1742
SAk3	0.014	0.125	1000	5.68	0.228	753
SASe	0.014	0.125	κ_{Se}	0.276	56.03	16000*
SABr	0.014	0.125	κ_{Br}	0.364	47.72	16000*
SATe	0.014	0.125	κ_{Te}	0.383	37.78	16000*
SAPd	0.014	0.125	κ_{Pd}	0.393	29.91	14500*
SAZr	0.014	0.125	κ_{Zr}	0.261	19.07	11000*
SACr	0.014	0.125	κ_{Cr}	1.093	13.11	8500*
SACe	0.014	0.125	κ_{Ce}	3.779	2.61	5500*
SASm	0.014	0.125	κ_{Sm}	4.973	2.60	1400*
SANd	0.014	0.125	κ_{Nd}	6.388	1.23	1200*
SAU	0.014	0.125	κ_{U}	3.008	4.42	1700*
SAw1	0.014	0.125	κ_{wind1}	0.295	21.09	16000*
SAw2	0.014	0.125	κ_{wind2}	0.402	30.82	16000*
SAd	0.014	0.125	κ_{dyn}	3.335	3.32	1400*

(*) Temperature of a blackbody spectrum with the closest fit (as a function of wavelength λ).

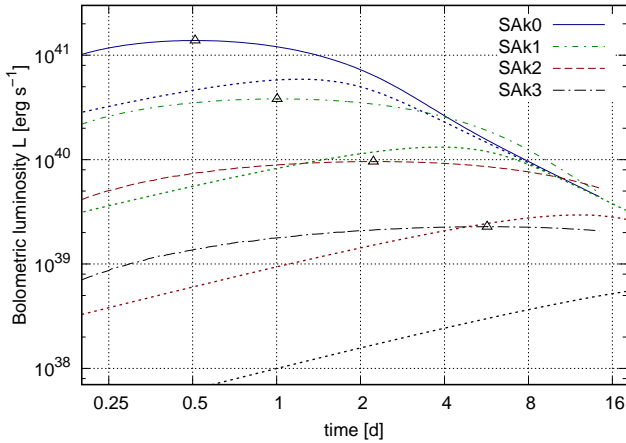


Figure 8. Bolometric luminosity for the analytic spherically-symmetric density distribution models SAK0 – SAK3, computed with SuperNu (thick solid and dashed lines), compared to luminosity estimates based on grey-opacity Grossman models (thin dotted lines). Black triangles indicate luminosity maxima.

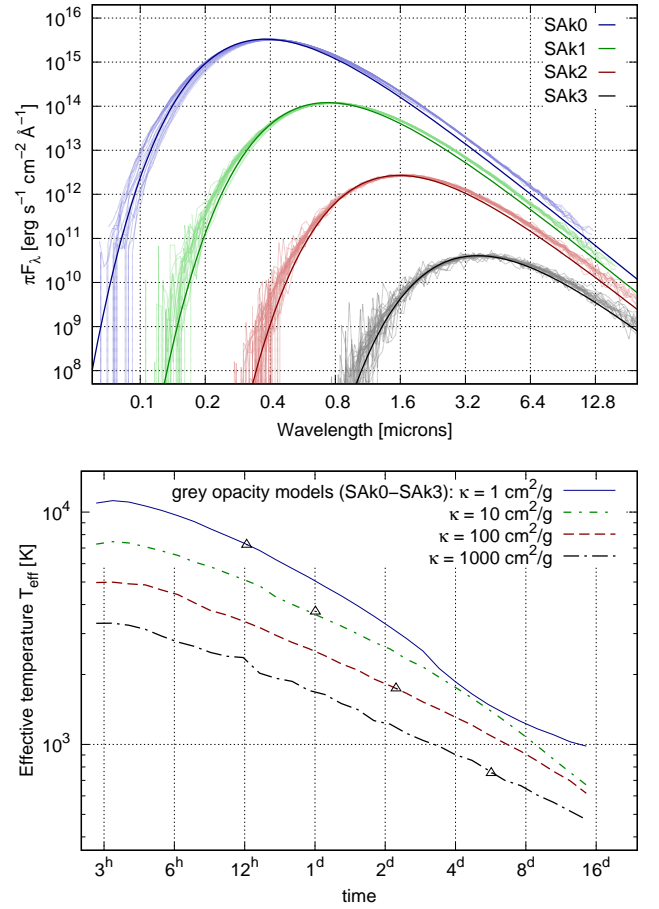


Figure 9. Top: spectra of grey-opacity spherically-symmetric analytic models SAK0 – SAK3 overplotted with best-fit blackbody spectra. Bottom: temperature evolution for the same four models, calculated from fits to the blackbody spectra. Triangles mark temperatures at the epochs of the peaks.

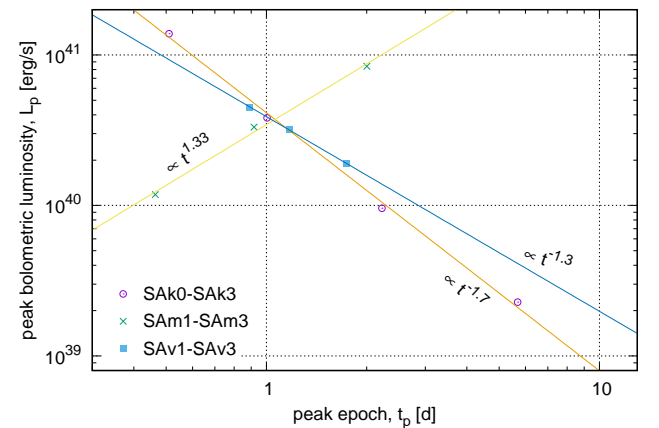


Figure 10. Peak luminosities L_p plotted against peak epochs t_p for models with varying grey opacities SAK0–SAK3, masses SAm1–SAm3 and velocities SAV1–SAV3, and corresponding power law fits.

$T_p \cdot \lambda_{\max} = 0.28977 \text{ cm} \cdot \text{K}$. The spectrum is wider than Planck by $\Delta\lambda/\lambda \approx 0.1$, which corresponds to a Doppler shift with the characteristic expansion velocity. Thus, the spectral evolution in the grey opacity models can be well described with a single evolution variable, such as effective temperature $T_{\text{eff}}(t)$, as shown in Fig. 9 (bottom).

Figure 10 illustrates behaviour of peak epochs and luminosities for models with varying ejecta masses, expansion velocities and opacities in $t_p - L_p$ plane. Combining these individual fits, we obtain the following expressions for the peak epoch, peak bolometric luminosity and effective temperature at the peak:

$$t_p = 1.0 \text{ d } \kappa_{10}^{0.35} M_2^{0.318} v_1^{-0.60}, \quad (27)$$

$$L_p = 2.8 \times 10^{40} \text{ erg s}^{-1} \kappa_{10}^{-0.60} M_2^{0.426} v_1^{0.776}, \quad (28)$$

$$T_p = 3720 \text{ K } \kappa_{10}^{-0.33} M_2^{-0.055} v_1^{0.011}. \quad (29)$$

and $M_2 := M_{\text{ej}}/10^{-2} M_{\odot}$, $v_1 := \frac{v_{\max}/2}{0.1c}$, $\kappa_{10} := \kappa/10 \text{ cm}^2 \text{g}^{-1}$.

These fits are qualitatively similar to semianalytic scaling laws derived in Grossman et al. (2014):

$$t_p = 4.9 \text{ d } \kappa_{10}^{0.5} M_2^{0.5} v_1^{-0.5}, \quad (30)$$

$$L_p = 2.5 \times 10^{40} \text{ erg s}^{-1} \kappa_{10}^{-0.65} M_2^{0.35} v_1^{0.65}, \quad (31)$$

$$T_p = 2200 \text{ K } \kappa_{10}^{-0.41} M_2^{-0.16} v_1^{-0.08}. \quad (32)$$

If peak magnitude is computed for a model with given ejecta mass m_0 , expansion velocity v_0 and opacity κ_0 , then similar empirical fits can be used to find peak parameters for a model with a different mass m_{ej} , velocity v and opacity κ . In particular, we find the following trends for wavelength bands:

$$\begin{aligned} m_g &= m_{g,0} - 1.13 \log_{10} m_{\text{ej}}/m_0 - 1.28 \log_{10} v/v_0 + 2.65 \log_{10} \kappa/\kappa_0 \\ m_r &= m_{r,0} - 1.01 \log_{10} m_{\text{ej}}/m_0 - 1.60 \log_{10} v/v_0 + 2.27 \log_{10} \kappa/\kappa_0 \\ m_i &= m_{i,0} - 0.94 \log_{10} m_{\text{ej}}/m_0 - 1.52 \log_{10} v/v_0 + 2.02 \log_{10} \kappa/\kappa_0 \\ m_z &= m_{z,0} - 0.94 \log_{10} m_{\text{ej}}/m_0 - 1.56 \log_{10} v/v_0 + 1.87 \log_{10} \kappa/\kappa_0 \end{aligned} \quad (33)$$

$$\begin{aligned} m_y &= m_{y,0} - 0.93 \log_{10} m_{\text{ej}}/m_0 - 1.61 \log_{10} v/v_0 + 1.76 \log_{10} \kappa/\kappa_0 \\ m_J &= m_{J,0} - 0.93 \log_{10} m_{\text{ej}}/m_0 - 1.61 \log_{10} v/v_0 + 1.56 \log_{10} \kappa/\kappa_0 \\ m_H &= m_{H,0} - 0.95 \log_{10} m_{\text{ej}}/m_0 - 1.55 \log_{10} v/v_0 + 1.33 \log_{10} \kappa/\kappa_0 \\ m_K &= m_{K,0} - 0.99 \log_{10} m_{\text{ej}}/m_0 - 1.53 \log_{10} v/v_0 + 1.13 \log_{10} \kappa/\kappa_0 \end{aligned}$$

Magnitudes and peak times for all our models are listed in tables given in Appendix B.

3.2 Semianalytic models: multigroup opacity

As a next step, we replace grey opacities with multigroup LTE opacities, calculated for the representative r-process elements listed in Table 2. Fig. 11 shows bolometric and broadband light curves for all non-grey models from Table 4, in the LSST *gri*zy and 2MASS *JHK* bands. The apparent variety of broadband light curves can be classified into three types: (i) bright early blue transients, peaking in optical bands on a timescale of a few hours (Fig. 11c); (ii) intermediate red transients, featuring double peaks in the *izy* bands on a timescale of a day or two (Fig. 11e,b), and (iii) late near-infrared (nIR) transients, showing very little emission in optical and peaking in *HK* bands on a timescale of a week (Fig. 11d,f). The difference in behavior originates from electronic configurations of the outer shells of corresponding elements, generating opacities that differ by orders of magnitude. These types correspond to the elements with open *p*-shell, *d*-shell and *f*-shell. Indeed, the first type includes

models with elements Se, Te and Br, which only have electrons in the outer *p*-shell in both neutral and the few first ionization stages that we consider. The second type includes Cr with outer shell configuration $3d^5 4s^1$, Zr with $4d^2 5s^2$ and Pd with closed outer *d*-shell $4d^{10}$ in a neutral state, but open *d*-shell in ionized states. The third type includes lanthanides Sm, Ce and Nd and actinide U, all with open *f*-shell. A higher orbital quantum number increases the amount of bound-bound transitions, and, consequently, opacity, by an order of magnitude, causing the computed qualitative differences in the light curves. Numerical values of peak times and peak magnitudes for each band and each spherically-symmetric model can be found in Table B1,

Bolometric light curves shown in Fig. 11, panel (a), also exhibit distinctive features that allow them to be classified into one of the three types. The three brightest models (Se, Br, Te) have a single peak at $t_p \sim 6^h$. Models with open *d*-shell elements (Cr, Pd, Zr) are a factor of a few dimmer, last longer ($\sim 1^d$) and show an extended plateau or a second peak in bolometric luminosity. Finally, models with open *f*-shell are more than one order of magnitude dimmer with a distinct rising phase and a peak at $t_p \sim 4^d - 8^d$.

The model with Ce stands out among open *f*-shell models with its early bright peak around $t_p \sim 0.15^d$. As can be seen on Fig. 11, panel (d), optical light curves for this model have a peak which is much brighter than for other open *f*-shell models shown on panel (f). Going back to the opacity plot (Fig. 6 in Sect. 2.3, bottom panel) we can see how this can be explained by element Ce having almost two orders of magnitude lower smeared opacity in blue optical wavelengths than other open *f*-shell elements. At late time (around one week) the light curve for Ce has a second peak in nIR *HK* bands just like other lanthanide/actinide-based models.

The two bottom panels of Fig. 11 show the light curves for mixed compositions: two types of wind (SAw1, SAw2) and dynamical ejecta SAd (see Table 2 for their composition details). These are shown in comparison with the two models with grey opacity: SAK0 for winds, and SAK1 for the ejecta. In all cases, the light curves of mixed models resemble those of the elements with the highest opacity: the light curves of wind models are closest to Zr and Cr, while the light curves for dynamical ejecta are closest to the ones of U and Sm. Note that our prescription for the opacity of mixed compositions by simple mass-weighted approach, detailed in Sect. 2.3, is probably an underestimate. In reality, highly opaque elements dominate the opacities even if present in very small amounts (see discussion on this topic in Sect. 6 in Kasen et al. 2013).

It is instructive to compare light curves of multigroup opacity models with those of grey opacity models, and try to infer an "effective opacity" that can be used as a simple approximation for the wind and dynamical ejecta models. Previous works (e.g., Rosswog et al. 2017; Grossman et al. 2014) used $\kappa = 10 \text{ cm}^2 \text{g}^{-1}$ for dynamical ejecta and $\kappa = 1 \text{ cm}^2 \text{g}^{-1}$ for wind outflows. Bolometric luminosities of wind and dynamical ejecta models (SAw1, SAw2 and SAd in Fig. 11a), can be compared with grey opacity models (displayed as shaded areas on the same plot). As can be seen from the plot, the wind models agree with the $\kappa = 1 \text{ cm}^2 \text{g}^{-1}$ model very roughly, only up to a factor of a few. Luminosity in dynamical ejecta model SAd is suppressed compared to $\kappa = 10 \text{ cm}^2 \text{g}^{-1}$ grey model at early times, but matches with the grey model at the peak, which is the time most relevant for detectability.

On the other hand, as pointed out in Dessart et al. (2016), using effective grey opacity produces inaccurate results, which can differ from detailed multigroup calculations by as many as 50 %, both in luminosity, and in peak time. In general, uniform effective opacity underestimates the opacity in the remnant core, which makes it

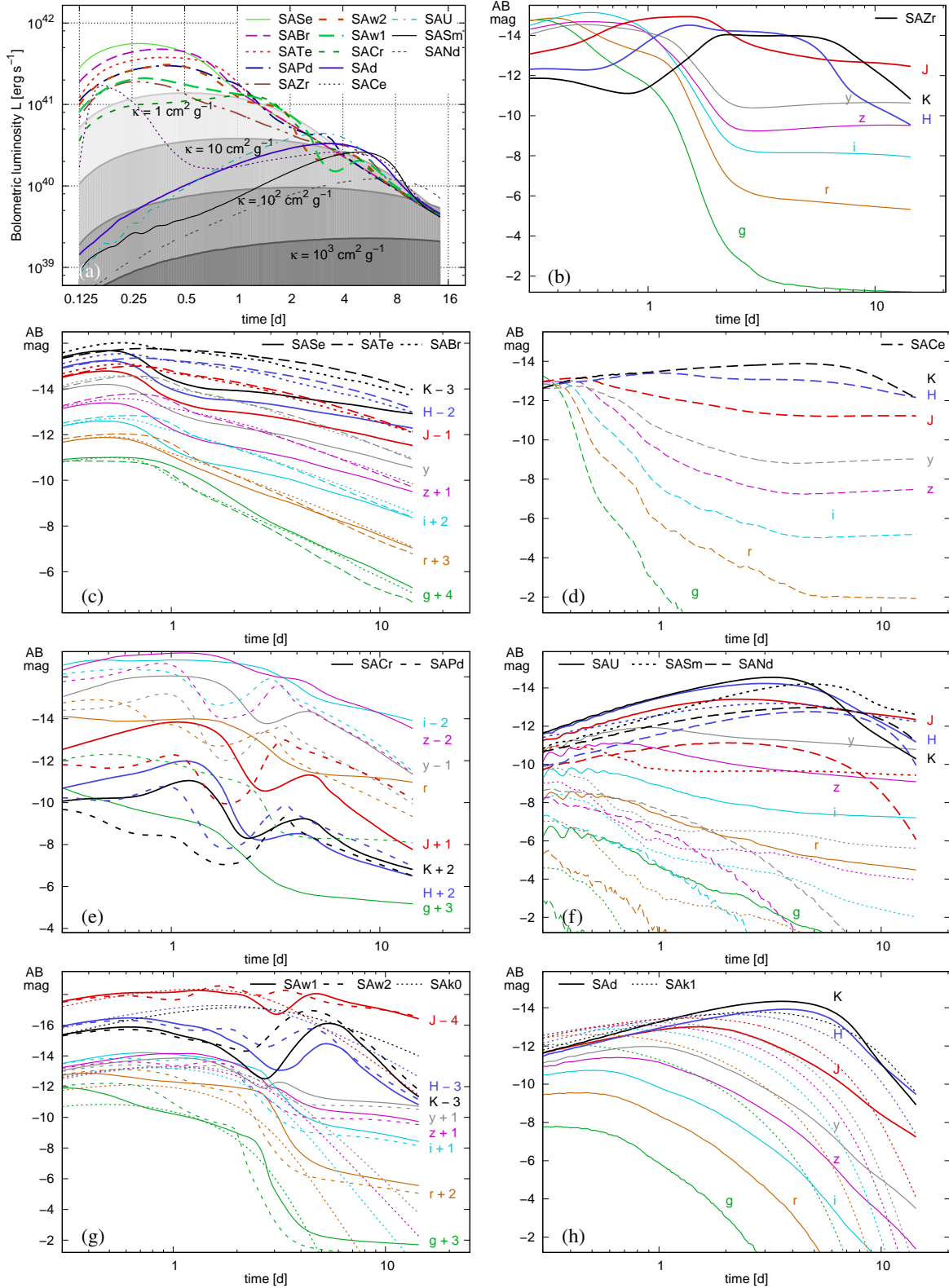


Figure 11. Bolometric (a) and broadband light curves (b-h) for models with spherically-symmetric analytic (SA*) density distributions and multigroup LTE opacities for single-element plasma (indicated by the remaining letters in abbreviations: Se, Br, Te, Pd, Zr, Cr, Ce, U, Sm or Nd), and mixed composition for dynamical ejecta (SAd) and two types of wind (SAw1 and SAw2). See elemental composition for the mixed models in Table 2. The shades of grey in panel (a) indicate bolometric light curves of the grey opacity models SAK0 – SAK3. Different bands are denoted with different colors. The light curves in the right column in panels (c), (e) and (g) are offset up or down to make the figures easier to read. Each band is offset by the same integer, shown on the right, e.g. "K – 3" indicates that the light curve in the *K* band is shifted upward by 3 mag.

transparent earlier and thus leads to earlier peaks (see Dessart et al. 2016).

As can be seen from the two bottom panels of Fig. 11, this effective opacity analogy can only be reasonably extended for the wind models SAw1 and SAw2, but not for the dynamical ejecta model. More specifically, the light curve of the dynamical ejecta model SAd only agrees with the grey model SAK1 in the infrared H and K bands. The analogy fails in optical bands and in the J band: for instance, the flux for the SAd model in the y band (Fig. 11h) around $t \sim 4^d$ is almost four magnitudes dimmer than what is predicted by the effective opacity. This behavior is attributed to a peculiar "spectral cliff" in the f -shell elements spectra, leading to abrupt suppression of the optical bands. This is explained in more detail in the analysis of the spectra below.

Figures 12–13 present corresponding spectral evolutions for each model in terms of luminosity per wavelength, $dL_\lambda/d\lambda$ (in units of $\text{erg s}^{-1} \text{ \AA}^{-1}$). Note that the spectra on these plots, for a time t , are shown shifted by a time-dependent constant $\text{const}(t) = -\log_2 t[d]$, positive for $t < 1^d$, negative for $t > 1^d$ and vanishing at one day. This gives a clearer picture of the evolution of spectral shapes as time progresses from top to bottom of the plot, forming a "spectral landscape" in the $\{\lambda, t\}$ -space. Thin grey lines on the plots show Planck spectra for a range of temperatures. Finally, to assist with comparing the spectra, we added charts showing the composition for mixed model plots.

Spectra for all models are similar to the blackbody spectrum in the sense that there is just one maximum with a steep rise at short wavelengths and a gradual $\propto \lambda^{-4}$ power law decay (Rayleigh-Jeans law) at long wavelengths. This shape is indented with broad spectral features, but no distinct lines or multiple peaks are present. One important feature in the spectra of f -shell elements (and to some extent d -shell elements) is the presence of a peculiar "spectral cliff" at late times, where the blue part of the spectrum is very strongly suppressed past a certain wavelength (for instance, around 1.6 microns for Sm). This is what leads to a drastic difference of the light curves in optical bands and even in the J band in comparison with the grey opacity models.

Models with p -shell elements Se, Br and Te do not have this feature at all, but rather exhibit very smooth spectra, which is close to Planck, with only a few spectral features (see Fig. 12, all plots in blue color). Models with elements with open d -shells (plots in green color in Fig. 12) have much more distorted spectra that are suppressed in UV. One particular opacity feature seen in nIR at wavelengths around $2 - 3 \mu\text{m}$ at the times about $\sim 1^d$ is responsible for the second peaks seen in the nIR light curves in Fig. 11b,e.

Figure 13 shows spectral evolution for lanthanides and actinide U (all plots in red color). Spectra of models with U, Nd and Sm are completely suppressed in UV and strongly suppressed in optical bands. This is due to much higher opacity in optical, which also explains why these three models do not have a plateau in bolometric luminosity compared to grey opacity models. (see Fig. 11a). Instead, the models exhibit a gradual increase in bolometric luminosity as the remnant cools and its thermal radiation moves to longer wavelengths where the opacity is lower.

In the nIR and IR, spectra of lanthanide and actinide models deviate from the Rayleigh-Jeans power law, while also displaying persistent wavelike patterns, unique for each element. An interesting observation is that for three out of four f -shell elements, the peak in the spectrum, which is generally expected to evolve towards longer wavelengths, does the opposite at times $t > 4^d$. These models essentially become slightly bluer at late epochs, which is a distinctive feature that can potentially be exploited to identify macronovae.

The model with Ce, possessing the simplest electronic structure among the lanthanides considered, initially has a spectrum which extends through the optical range all the way to UV (see Fig. 13, top left). However, after $t > 1^d$ the spectrum starts behaving similarly to the other lanthanide spectra.

Figure 12 (bottom row) shows spectral evolution of mixed wind models. Both wind models look very similar and closely resemble the spectral evolution of the Zr model (top left panel in Fig. 12). This is remarkable considering that in model SAw1, for Wind 1, only $\sim 1.3\%$ of Zr is present. The mixed dynamical ejecta model SAd is presented in the bottom plot of Fig. 13. Just like with the wind models, the elements with the highest opacity dominate the spectrum: the dip around $\lambda = 2$ microns specific to Sm and the wave-like pattern of Nd both can be seen at the late epochs of SAd spectra, while no spectral feature of Te can be found, despite the fact that it constitutes $> 80\%$ by mass.

3.3 Dynamical ejecta: spherical symmetry and axisymmetry

In this section we turn our attention away from composition and focus on the impact of morphology. To simplify the comparison between the models while keeping a certain level of realism, we use detailed multigroup opacities of Sm in all of our models, which is the lanthanide that was explored in previous works (Fontes et al. 2015a, 2017). Consideration of just the dynamical ejecta models is also motivated by the fact that, under certain conditions in Nature, secondary wind outflows can be completely subdominant: either being obscured by dynamical ejecta, or having too low mass, or too slow expansion velocity. Thus, results of this section can be used for constraining theoretical models in which the wind outflow is not present or can be neglected. By focusing on dynamical ejecta only, we can explore the effects of the spatial distribution of the ejecta and their orientation with respect to the observer.

Parameters of our models are summarized in Table 5, and averaging is described in Sect. 2.1.2. Table 5 also lists peak parameters of the bolometric light curves and the H band magnitudes. The different types of averaging of the 3D SPH distribution are indicated by suffixes: "2d" (axisymmetric models), "1d" (axisymmetric models integrated vertically) and "1dm" (axisymmetric models averaged with respect to the local density maximum in the equatorial plane). As can be seen from Table 5, different types of averaging result in different median expansion velocities. Models A1dSm–D1dSm possess the highest expansion velocity, models averaged around local density maximum, A1dmSm–D1dSm, have the lowest expansion, and axisymmetric models have expansion velocities somewhere in between. As expected from scaling formulae (27, 28), slower expansion produces dimmer light curves that peak later in time.

Figure 14 shows bolometric light curves for these models, along with two models studied in previous sections: SASm with analytic radial density profile, and SAK1 with the grey opacity $\kappa = 10 \text{ cm}^2 \text{ g}^{-1}$. Several common trends, which reveal the impact of morphology, can be identified. For a fixed mass and average density, spherical configurations should give the dimmest possible transients in terms of bolometric power radiated in all directions. This is due to the lowest possible geometric area of the photosphere, which keeps the maximum amount of generated heat from escaping. For the same reason, equivalent ejecta masses with denser distributions are expected to produce later peaks. Vice versa, more flattened and irregular matter distributions would produce brighter and earlier signals (from orientations or "views" with a sufficiently large projected photosphere area). In accord with previous works (Grossman et al. 2014), on-axis orientations produce a transient which is brighter than for

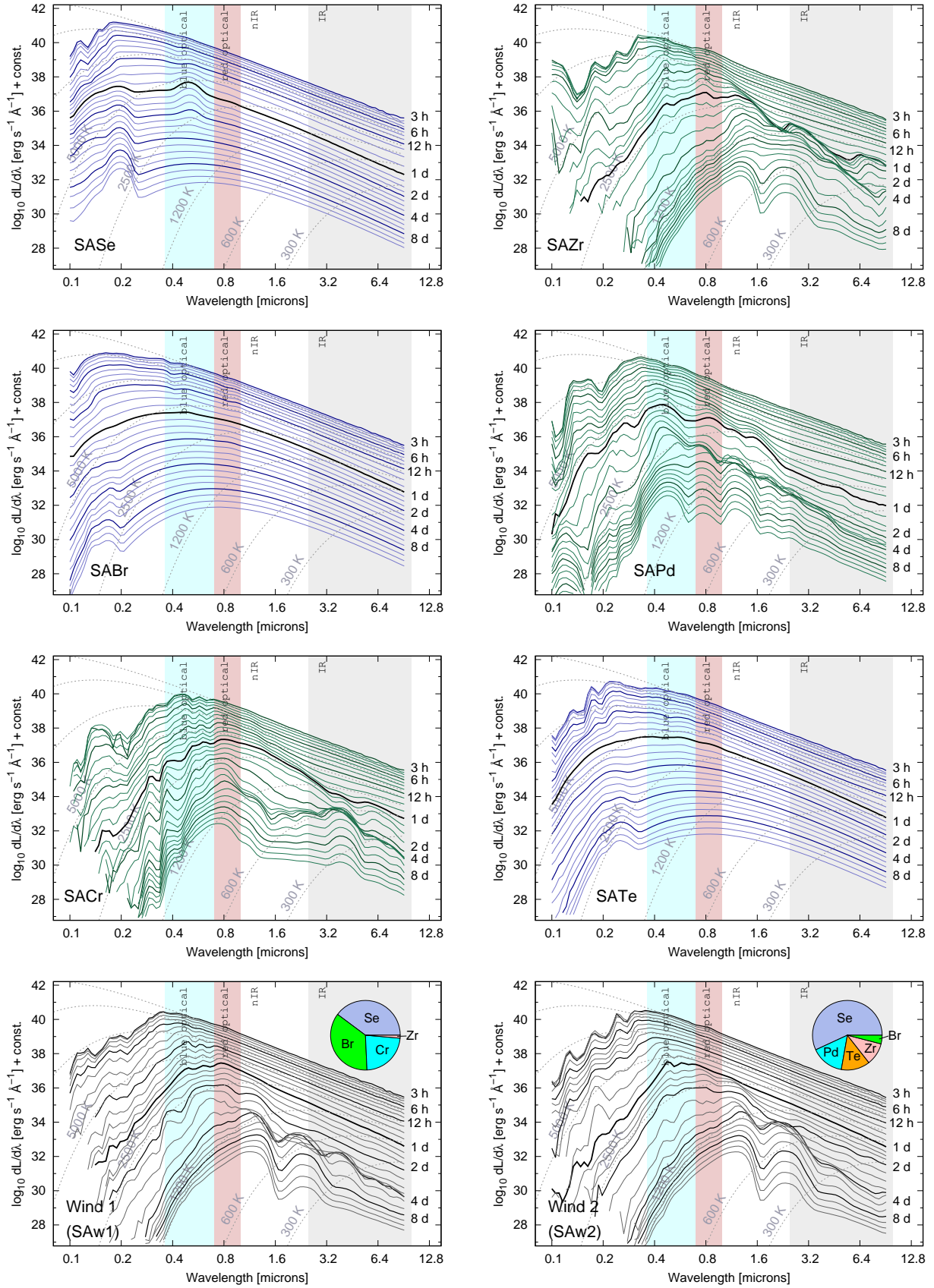


Figure 12. Evolution of macronova spectra for spherically-symmetric models with LTE opacities formed by lighter non-lanthanide elements Se, Te, Br, Pd, Zr, Cr and two types of wind, representing their mixture: SAw1 and SAw2 (see Table 4). For clarity, spectral curves for different times are offset by $\text{const.}(t) = -\log_2 t$ [d] (i.e. no offset for $t = 1$ day). Thin dashed lines show blackbody spectra for a range of temperatures.

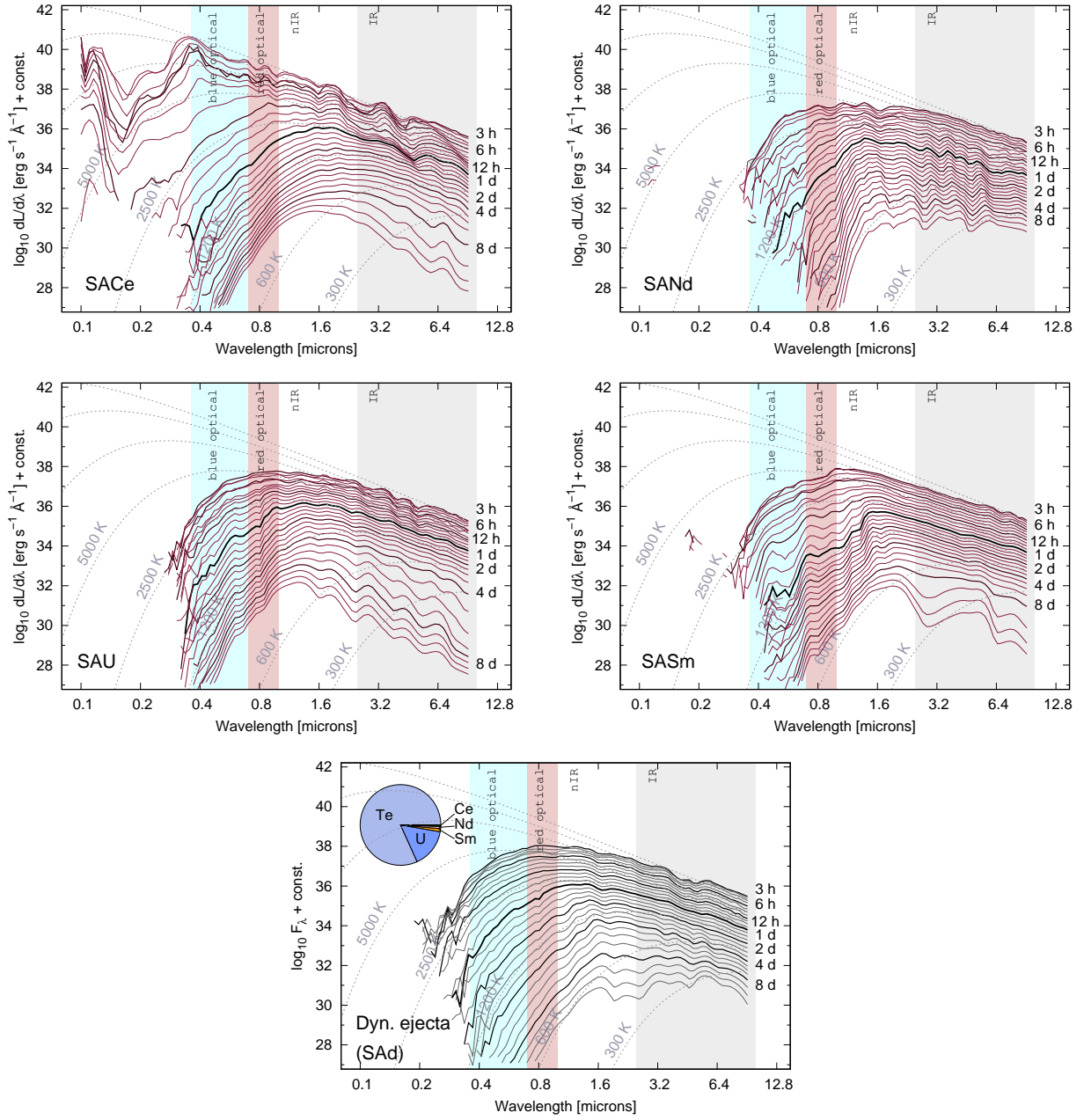


Figure 13. Evolution of macronova spectra for models with LTE opacities of lanthanides Ce, Nd, Sm, actinide U, and dynamical ejecta mixture. (see Table 4). Spectra for different times t are shifted by a time-dependent constant $\text{const.}(t) = -\log_2 t[\text{d}]$. Thin dashed lines show blackbody spectra for a range of temperatures.

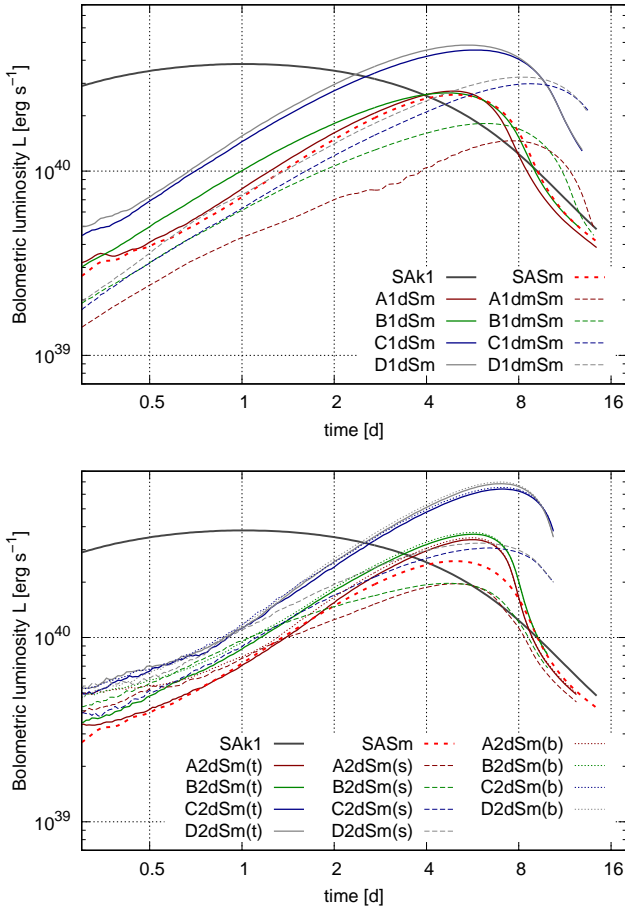


Figure 14. Top: time evolution of bolometric luminosity for spherically-symmetric dynamical ejecta models A1dSm-D1dSm and A1dmSm-D1dmSm (top) which use detailed opacity of Sm (see Table 5). Bottom: same for axisymmetric models A2dSm-D2dSm as observed on-axis ("t" for "top view", "b" for bottom view) and "from the side" ("s"). Models SASm and SAk1 are shown for comparison.

a "side" orientation by a factor of 2-3. Both types of 1D-models fall within the range between the brighter "top/bottom" and dimmer "side" orientations of the corresponding 2D-models. This orientation effect simply reflects the difference in the area of photosphere projection on the view plane, which is higher for the on-axis case. The light curve of the SASm model, which has a slightly different density profile but the same mass and expansion velocity as A1dSm, agrees with the light curve of A1dSm very well, demonstrating that the exact shape of the density profile does not have a significant effect.

Our dynamical ejecta configurations are not symmetric with respect to reflection in the equatorial plane; therefore there is a small difference between the "top" and "bottom" views. Although this difference is negligible for pure dynamical ejecta models, it becomes substantial once the wind component is added (see Sect. 3.4 below). The light curve of the grey opacity model SAk1 roughly agrees in its bolometric luminosity with A/B-models in the vicinity of the peak, but shows much brighter values for $t < 2^d$. This is because our dynamical ejecta models, calculated with the detailed opacity of Sm, are strongly suppressed in the optical part of the spectrum. Even though at times $t < 2^d$ the temperature in the radiative layer produces blackbody spectra peaking in the optical, this radiation is

Table 5. Models of dynamical ejecta (based on merger simulations). Columns specify: total ejecta mass, median velocity, bolometric peak time, peak bolometric luminosity, time of peak in the H band and maximum magnitude in the H band. All models in this table use detailed opacities of Sm. In the last block of models (2d-models), a letter in brackets indicates viewing angle: "t" for top view, and "s" for side view (bottom view is almost identical to the top view for these models).

Model	M_{ej} [M_{\odot}]	$\bar{v}_{1/2}$ [c]	t_p [d]	L_p [$10^{40} \frac{\text{erg}}{\text{s}}$]	t_H [d]	m_H [mag]
A1dSm	0.013	0.132	4.877	2.72	3.34	-13.3
B1dSm	0.014	0.125	4.669	2.66	2.77	-13.3
C1dSm	0.033	0.132	5.758	4.55	2.88	-13.7
D1dSm	0.034	0.136	5.457	4.83	2.87	-14.0
A1dmSm	0.013	0.066	7.630	1.46	5.17	-12.4
B1dmSm	0.014	0.080	6.230	1.81	3.72	-12.7
C1dmSm	0.033	0.055	8.723	2.98	5.49	-13.1
D1dmSm	0.034	0.058	8.202	3.24	4.67	-13.2
A2dSm(t)	0.013	0.095	5.650	3.40	4.47	-13.3
A2dSm(s)			5.007	1.99	3.33	-13.1
B2dSm(t)	0.014	0.086	5.671	3.65	4.37	-13.4
B2dSm(s)			4.783	1.98	2.57	-13.2
C2dSm(t)	0.033	0.119	7.083	6.40	4.98	-13.9
C2dSm(s)			6.407	3.10	3.36	-13.6
D2dSm(t)	0.034	0.121	6.982	6.85	5.20	-14.0
D2dSm(s)			5.999	3.30	3.30	-13.8

strongly suppressed on the way out compared to the grey opacity models. As the remnant cools down with time due to expansion, the peak of thermal emission shifts into infrared where the opacity is much lower. Later, at $t \sim 4^d - 8^d$ the light curves of A/B-models catch up and even exceed the bolometric luminosity of the grey opacity model with $\kappa = 10 \text{ cm}^2 \text{ g}^{-1}$.

Even this rough agreement between the grey opacity light curve and the Sm-opacity models in the bolometric case breaks down if we consider broadband light curves, similar to the discrepancy pointed out in Sect. 3.2. Due to the presence of the "spectral cliff" in open f -shell element models, all *grizy*- and J -band light curves are strongly suppressed in comparison to the grey opacity model. This is shown in Fig. 15, bottom right panel, which displays broadband light curves for models A2dSm, A1dSm and the grey opacity model SAk1. All the light curves except for the longest-wavelength H and K bands are suppressed by more than 3 mags. Other panels in Fig. 15 demonstrate snapshots of spectra for model A2dSm at different times for different viewing angles, and the "spectral cliff" at around 1.6 microns (in the middle of the H band) can be clearly identified. The rest of the dynamical ejecta models from Table 5 show very similar spectral evolution and light curves.

An interesting morphological effect reveals itself in Fig. 15 when comparing the spectra of 2D model A2dSm with corresponding spherically-symmetric 1D case A1dSm. At early epochs $t < 1^d$, the 2D model has non-negligible contributions in the optical and even UV parts of the spectrum, absent in the 1D spectra. Moreover, this feature is more pronounced for the on-axis orientations relative to the "side" view. In other words, the merger remnant appears "bluer" in color if shaped in toroidal form as opposed to the same mass arranged in a spherical configuration. This is manifest in the *grizy* bands, as shown in the bottom right panel of Fig. 15: light curves of 2D models are initially brighter than 1D models by almost 1 mag.

This effect can be explained if we recall that the remnant spectrum is shaped by thermal emission originating from the depths of the remnant and viewed through a layer of semi-opaque material, which dents the original Planck spectrum with its opacity profile.

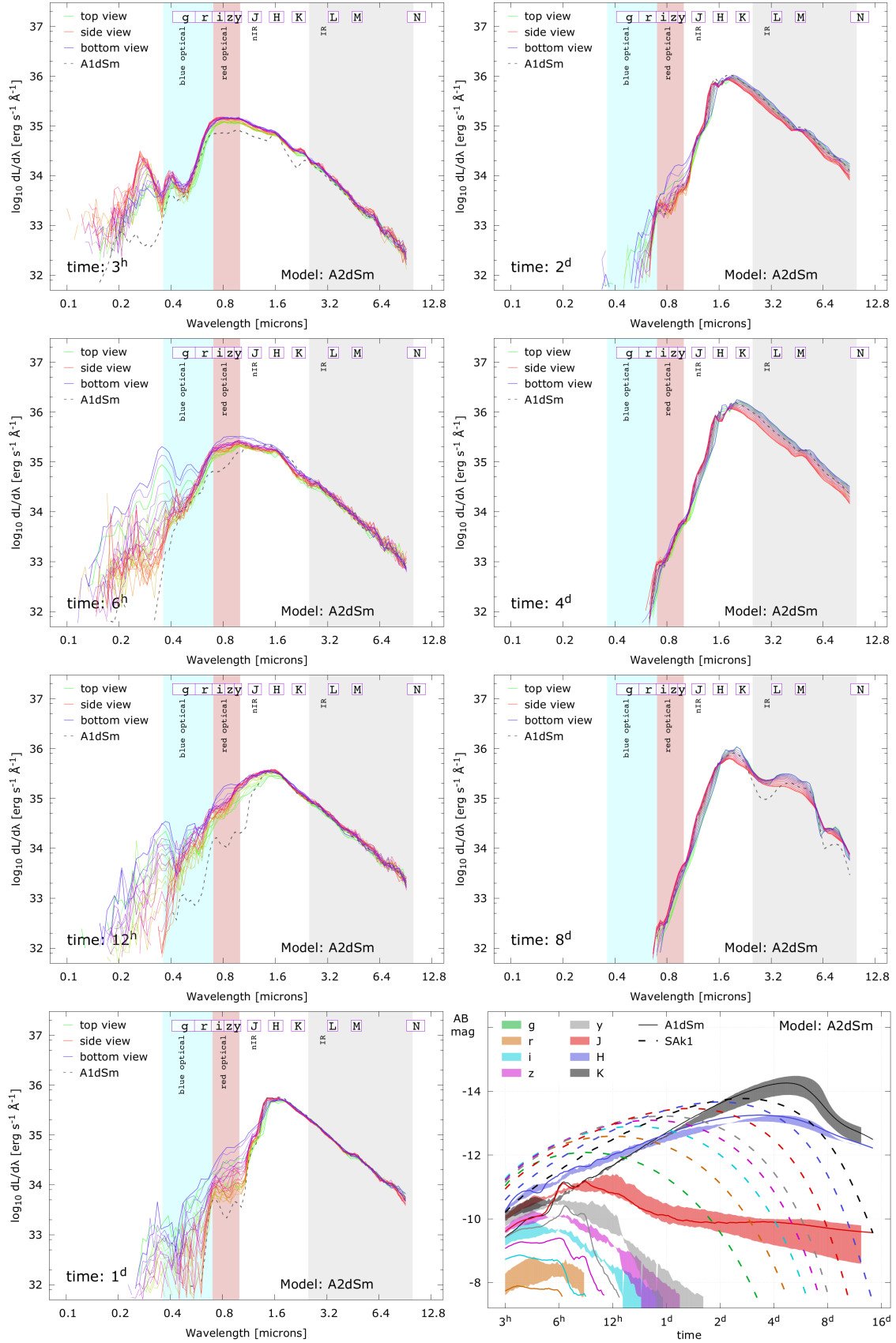


Figure 15. Time evolution of synthetic spectra for models A2dSm and A1dSm. Bottom right: broadband light curves for model A2dSm for two different orientations (colored ranges) with respect to the observer, compared to the broadband light curves for the grey opacity model SAK1 with $\kappa = 10 \text{ cm}^2 \text{ g}^{-1}$ (dashed lines) and spherically-symmetric averaged model A1dSm (solid lines). Note that the light curve in the g band for the grey opacity model reaches -12 mag, for models A1dSm and A2dSm it is far too dim and thus is not shown.

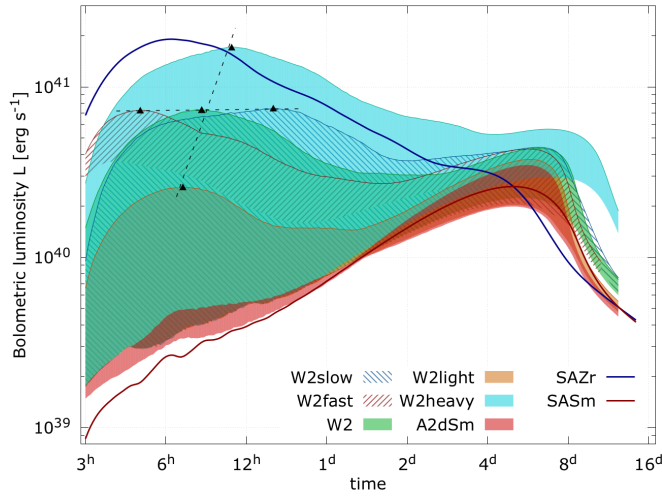


Figure 16. Range of bolometric luminosities for combined models with varying wind parameters: W2, W2light–W2heavy and W2slow–W2fast (see Table 6) spanned by different orientations with respect to the observer. Spherically-symmetric multigroup opacity models SAZr and SASm, corresponding to the composition of the wind and dynamical ejecta respectively, are shown for comparison. The axisymmetric dynamical ejecta model A2dSm, which is W2 without wind, is also shown. Upward triangles indicate locations of the blue transient peak, and dashed lines show peak trends with varying wind mass (semi-vertical) and velocity (horizontal line).

This layer has smaller optical depth for axisymmetric models, and as a consequence, the blue thermal emission is less suppressed on the way out. In an extreme case, if ejecta had a thin shell-like configuration, the spectrum would have been completely unsuppressed in the optical bands despite lanthanide contamination.

3.4 Combined models of wind and dynamical ejecta

Combined models (as introduced in Sect. 2.1.3) superimpose axisymmetric configurations of the dynamical ejecta with various parameterized spherically-symmetric profiles for the wind (see Fig. 1, bottom panel). These models were designed to assess visibility of a potential bright blue transient originating from the wind.

The first 14 entries in Table 6 list combined models (denoted with a prefix W2, "W" for "wind", and "2" for "2D-models"). The rest of the models in the Table improve on these models by adding more physics, and will be considered in the Sect. 4 below. For the purpose of comparison with previous sections, all W2-models are calculated with the multigroup opacity of Sm (same as for the model A2dSm). All models use dynamical ejecta configuration A, except for W2B, W2C and W2D, which use configurations B, C and D respectively. Opacity for the wind in models W2A–W2D and models W2heavy/W2light, W2fast/W2slow is the multigroup opacity of Zr, which was selected because it is the most opaque element shaping the spectra and light curves in mixtures (see Sect. 3.2).

Figure 16 displays bolometric luminosities for the baseline model W2, models departing from the baseline in wind mass W2light/W2heavy, and models departing from the baseline in wind expansion velocity W2slow/W2fast. The plot also shows comparative luminosities of A2dSm and single-element spherically-symmetric models SAZr and SASm with uniform composition, corresponding to that of the wind and ejecta only. To reflect the luminosity range due to different orientations, each 2D model is displayed as a stripe, with the upper stripe bound corresponding to the on-axis

view, and the lower bound showing the "side" view. At times $t < 1^d$, the on-axis luminosities approach those of SAZr, while the "side" view luminosities always stay close to SASm.

This illustrates the presence of a blue transient, associated with the wind. The transient is orientation-dependent, and clearly absent for "side" orientations, showing that the wind is completely obscured for this view. The on-axis configurations, on the other hand, display a peculiar double-peak structure, with the first, early blue peak at $t \sim 0.3^d$ generated by the wind outflow, and the second nIR peak at $t \sim 4^d$ generated by the dynamical ejecta.

Table 6 lists numerical values for the positions of both peaks in all 2D models, for the "top" and "bottom" orientations of the remnant. The "side" orientation is omitted, because it does not depend on the wind and thus is the same as in dynamical ejecta-only models A2dSm–D2dSm, considered in the previous section. In more than half of the cases in Table 6, the blue peak is missing or substantially suppressed in one orientation compared to the other. This is due to the irregular morphology of the ejecta around the axis and lack of symmetry with respect to reflection in the equatorial plane. Configuration of the dynamical ejecta density on the north and south poles of the remnant is different, causing the wind transient to be partially or completely obscured. In general, this gives an idea of how sensitive the blue transient wind signal is to the precise distribution of clumps in dynamical ejecta. Even though the density of dynamical ejecta around the axis is rather small, it can still interfere with the wind-generated transient.

Figure 16 also displays the location of the blue peak (black upward triangles) and its dependence on the wind mass and expansion velocity (dashed thin lines). Its behavior is qualitatively similar to expressions (27–28): more massive wind produces a later and brighter transient, and faster wind produces an earlier transient. Empirical fits for the peak times $t_{p,\text{wind}}$ and luminosities $L_{p,\text{wind}}$ give the following formulae:

$$t_{p,\text{wind}} = 0.32 \text{ d } M_{w,2}^{0.14} v_{w,1}^{-0.83}, \quad (34)$$

$$L_{p,\text{wind}} = 1.1 \times 10^{41} \text{ erg s}^{-1} M_{w,2}^{0.63}, \quad (35)$$

where $M_{w,2} := M_{\text{wind}}/10^{-2}M_{\odot}$ and $v_{w,1} := \frac{v_{\text{wind,max}}/2}{0.1 c}$ are rescaled mass and expansion velocity parameters of the wind. The power law indices in these expressions are different from the ones in (27–28) because of the presence of the dynamical ejecta. In particular, the luminosity of the wind peak is almost independent on the expansion velocity of the wind.

Models W2Se–W2Cr in Table 6 explore the effect of light element composition on the blue transient. It turns out to be surprisingly small: blue peak luminosities and peak epochs in Table 6 are largely unaffected by which specific element contributes to the wind. Fig. 17 shows the time evolution of angle-dependent spectra for our baseline combined model W2.

All models in this group show qualitatively similar spectral behaviour: the spectra at early times show pronounced dependence on the remnant orientation. The spectra in Fig. 17 clearly resemble the spectrum of the Zr models for on-axis orientations, and reduce to A2dSm-like spectra for side views. Several distinct spectral features of Zr can be clearly identified in the early on-axis spectra. At late times, the spectrum approaches that of dynamical ejecta-only model A2dSm for all orientations (which in turn is close to the model SASm).

Figure 18 shows corresponding angle-dependent AB magnitudes in the optical *grizy* and nIR *JHK* bands. Optical magnitudes reach values as high as -13 mag at $t \sim 0.3^d$, while nIR magnitudes peak on timescales of $t \sim 4 - 6^d$ with peak magnitudes around -14.5 .

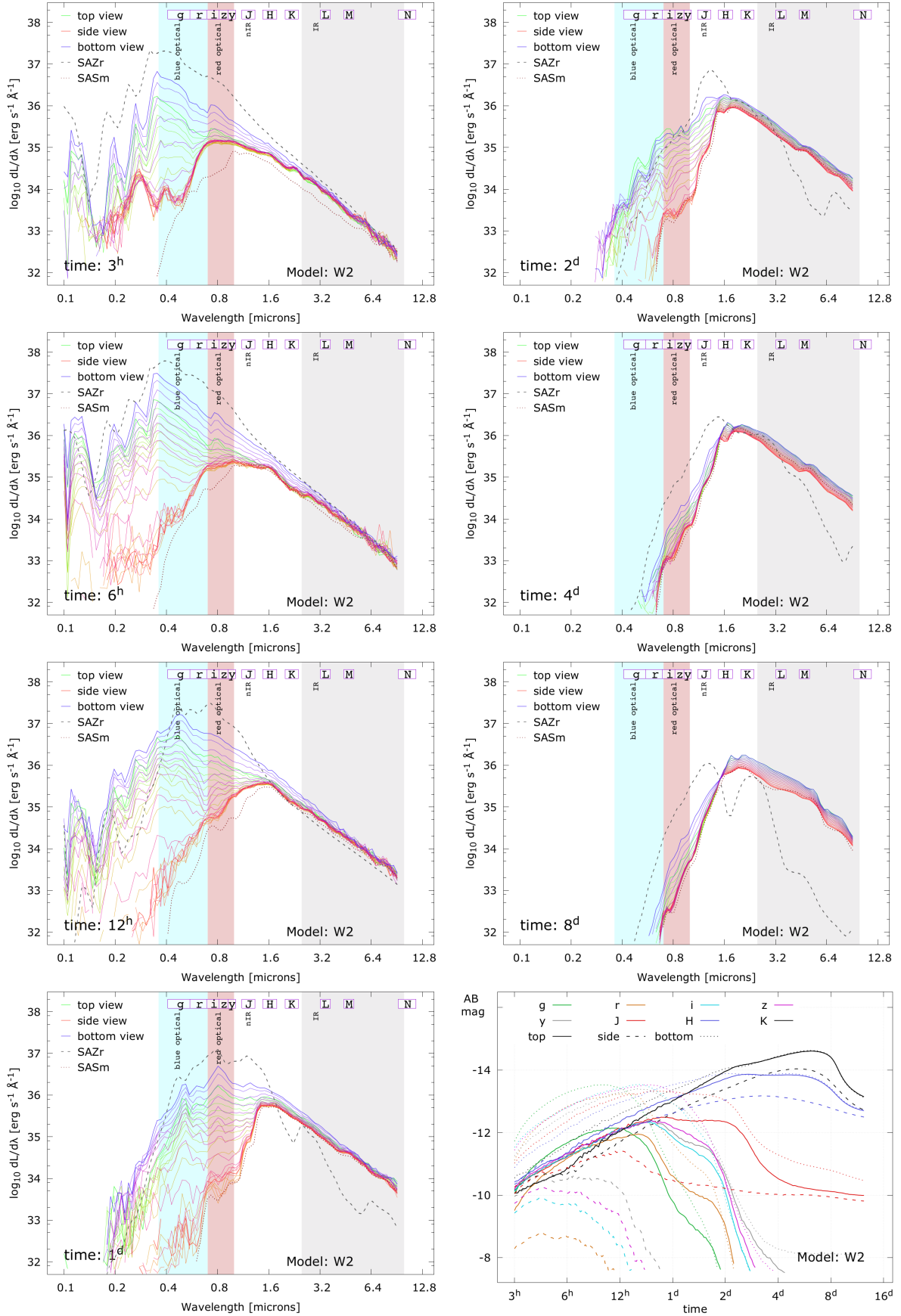


Figure 17. Time evolution of angle-dependent spectra for the baseline combined model W2 (also denoted as W2A or W2Zr). Bottom right: bolometric light curves of the same. Color gradient indicates polar angle θ , and spans 27 angular bins from "top" ($\theta = 0$, blue) to "bottom" ($\theta = \pi$, green), spaced equally in $\cos \theta$. The spike at $\lambda \sim 0.16$ at early times is unphysical and caused by artificial windows in our opacity profile at the same wavelengths.

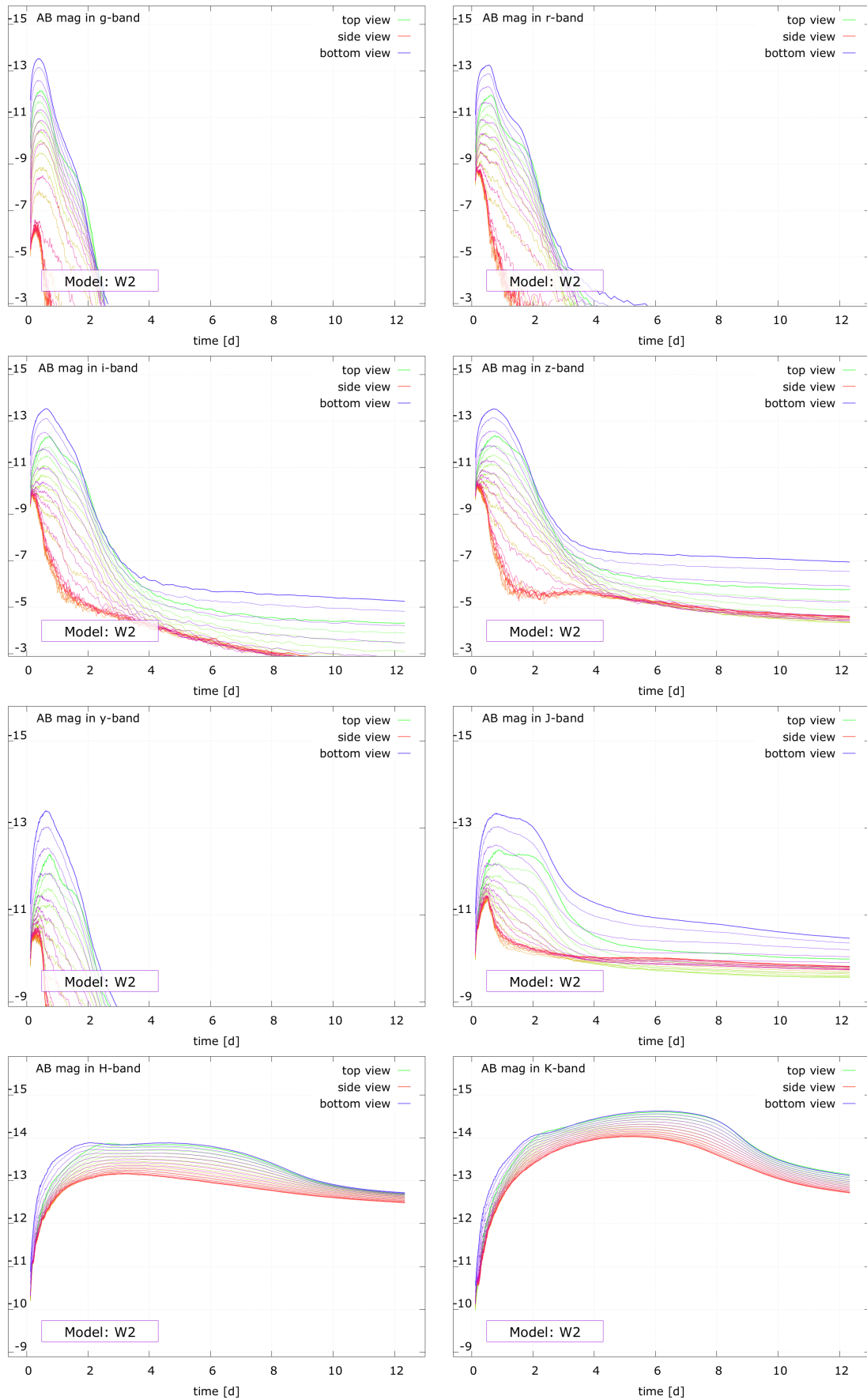


Figure 18. Broadband light curves for the optical *grizy* and nIR *JHK* bands for model W2. Color gradient is the same as in previous plot.

Table 6. Parameters of the combined axisymmetric models of dynamical ejecta and wind. First three columns list wind mass M_{wind} , half the maximum wind velocity $v_{\text{wind,max}}$ in the wind density profile (10), and opacity of the wind + dynamical ejecta. Masses and median velocities of the dynamical ejecta components A, B, C, D are listed in Table 5. For dynamical ejecta component in the W2-models we use detailed opacities of Sm ($\kappa_{\lambda,\text{Sm}}$). For dynamical ejecta in the rest of the models, we use a mix of detailed ejecta opacities, as described in Sect. 2.3.

Model	M_{wind} [M_{\odot}]	$v_{\text{wind}}/2$ [c]	opacity	top view				bottom view			
				$t_p^{(1)}$ [d]	$L_p^{(1)}$ [$10^{40} \frac{\text{erg}}{\text{s}}$]	$t_p^{(2)}$ [d]	$L_p^{(2)}$ [$10^{40} \frac{\text{erg}}{\text{s}}$]	$t_p^{(1)}$ [d]	$L_p^{(1)}$ [$10^{40} \frac{\text{erg}}{\text{s}}$]	$t_p^{(2)}$ [d]	$L_p^{(2)}$ [$10^{40} \frac{\text{erg}}{\text{s}}$]
W2A (W2)	0.005	0.08	$\kappa_{\text{Zr}} + \kappa_{\text{Sm}}$	0.48	2.429	6.24	4.266	0.34	7.309	6.20	4.366
W2B	0.005	0.08	$\kappa_{\text{Zr}} + \kappa_{\text{Sm}}$	-	-	5.93	4.102	-	-	5.93	4.162
W2C	0.005	0.08	$\kappa_{\text{Zr}} + \kappa_{\text{Sm}}$	0.38	1.990	7.24	6.788	-	-	7.20	6.898
W2D	0.005	0.08	$\kappa_{\text{Zr}} + \kappa_{\text{Sm}}$	-	-	7.08	7.208	-	-	7.02	7.324
W2Se	0.005	0.08	$\kappa_{\text{Se}} + \kappa_{\text{Sm}}$	0.49	4.873	5.93	4.389	0.35	13.92	5.78	4.546
W2Br	0.005	0.08	$\kappa_{\text{Br}} + \kappa_{\text{Sm}}$	0.65	4.260	5.94	4.387	0.44	11.67	5.80	4.531
W2Te	0.005	0.08	$\kappa_{\text{Te}} + \kappa_{\text{Sm}}$	0.85	3.702	5.94	4.386	0.51	9.931	5.80	4.525
W2Pd	0.005	0.08	$\kappa_{\text{Pd}} + \kappa_{\text{Sm}}$	0.65	3.292	5.93	4.388	0.48	9.227	5.80	4.537
W2Zr (W2)	0.005	0.08	$\kappa_{\text{Zr}} + \kappa_{\text{Sm}}$	0.48	2.429	6.24	4.266	0.34	7.309	6.20	4.366
W2Cr	0.005	0.08	$\kappa_{\text{Cr}} + \kappa_{\text{Sm}}$	-	-	5.91	4.408	1.62	4.437	5.76	4.557
W2light	0.001	0.08	$\kappa_{\text{Zr}} + \kappa_{\text{Sm}}$	0.33	0.980	5.78	3.673	0.29	2.583	5.75	3.755
W2heavy	0.02	0.08	$\kappa_{\text{Zr}} + \kappa_{\text{Sm}}$	0.94	5.949	6.91	5.518	0.44	17.09	6.79	5.653
W2slow	0.005	0.04	$\kappa_{\text{Zr}} + \kappa_{\text{Sm}}$	0.78	3.948	6.25	4.371	0.63	7.453	6.22	4.426
W2fast	0.005	0.16	$\kappa_{\text{Zr}} + \kappa_{\text{Sm}}$	0.20	7.287	5.73	4.225	0.21	5.786	5.69	4.327
X ₁	0.005	0.08	$\kappa_{\text{wind1}} + \kappa_{\text{dyn}}$	-	-	2.76	6.408	0.42	5.952	2.77	6.593
X ₂	0.005	0.08	$\kappa_{\text{wind2}} + \kappa_{\text{dyn}}$	-	-	2.54	6.247	0.56	7.576	3.73	6.184
DZ ₁	0.005	0.08	$\kappa_{\text{wind1}} + \kappa_{\text{dyn}}$	-	-	5.17	28.79	0.5*	11.0*	5.28	29.89
DZ ₂	0.005	0.08	$\kappa_{\text{wind2}} + \kappa_{\text{dyn}}$	-	-	5.24	27.92	0.5*	13.0*	5.28	28.97
Xnh ₁	0.005	0.08	$\kappa_{\text{wind1}} + \kappa_{\text{dyn}}$	0.69	4.041	4.29	6.893	0.40	11.08	4.23	7.094
Xnh ₂	0.005	0.08	$\kappa_{\text{wind2}} + \kappa_{\text{dyn}}$	0.62	9.499	2.77	10.14	0.42	25.87	2.8*	9.8*
γA_1	0.005	0.08	$\kappa_{\text{wind1}} + \kappa_{\text{dyn}}$	0.7*	4.4*	4.12	7.408	0.40	11.75	4.07	7.679
γB_1	0.005	0.08	$\kappa_{\text{wind1}} + \kappa_{\text{dyn}}$	-	-	4.25	7.615	-	-	4.25	7.705
γC_1	0.005	0.08	$\kappa_{\text{wind1}} + \kappa_{\text{dyn}}$	0.6*	3.9*	5.29	13.60	-	-	5.29	13.79
γD_1	0.005	0.08	$\kappa_{\text{wind1}} + \kappa_{\text{dyn}}$	-	-	5.30	14.12	-	-	5.29	14.31
γA_2	0.005	0.08	$\kappa_{\text{wind2}} + \kappa_{\text{dyn}}$	0.61	10.06	2.87	11.05	0.42	27.57	2.7*	10.8*
γB_2	0.005	0.08	$\kappa_{\text{wind2}} + \kappa_{\text{dyn}}$	-	-	4.28	9.422	-	-	4.37	9.363
γC_2	0.005	0.08	$\kappa_{\text{wind2}} + \kappa_{\text{dyn}}$	0.7*	6.2*	5.35	14.98	-	-	5.40	15.08
γD_2	0.005	0.08	$\kappa_{\text{wind2}} + \kappa_{\text{dyn}}$	-	-	5.33	15.47	-	-	5.40	15.57

(*) Distinct peak is missing in these models.

This clearly demonstrates the double-peak nature of the transient, as well as its dependence on orientation.

For references, Tables B2, B3, and B4 contains detailed information on peak magnitudes, epochs and transient durations for all optical and nIR bands, and for three orientations: top, bottom and side respectively.

4 MOVING TOWARDS REALISTIC MODELS

Previously, we approximated radioactive heating with a power law formula (18), and used a constant thermalization $\epsilon_{\text{th}} = 0.25$ to represent the fraction of this heating, which is converted to thermal energy. Here we lift these assumptions and exploit our knowledge about composition and radioactive decays in the outflows to make our models more realistic. By adding different ingredients one-by-one, we can gauge their individual impact.

In models X₁ and X₂, we take model W2 and replace the opacity of pure Sm in dynamical ejecta and Zr in the wind with the opacity mixtures from Table 2, similarly to the models SAd and SAw1/SAw2 for two types of wind. In Xnh₁ and Xnh₂ we replace analytic nuclear heating in X₁ and X₂ with detailed nuclear heating generated by radioactive decays, and add species-dependent thermalization, as explained in Sect. 2.2.

As pointed out in the end of Sect. 2.2, much of the nucleosynthesis

occurs close to the neutron dripline where experimental information is not available and one has to rely on theoretical models. The available nuclear mass models agree overall reasonably well, but they make different predictions for the amount of matter in the trans-lead region. Since the corresponding nuclei undergo alpha-decay, their amount seriously impacts the nuclear heating rate and "standard" mass formulae (e.g. FRDM vs DZ) can differ by as much as an order of magnitude in the predicted heating rates.

To explore the impact of nuclear heating on macronovae, we introduce models DZ₁ and DZ₂, which are identical to X₁ and X₂ except for the heating rate, which is higher by a factor of 10 to mimic the DZ heating rate. These models produces substantially brighter transients, as can be seen in Fig. 21 and the 2nd to last block of rows in Tables 6, B2, B3, and B4.

Our most sophisticated models, that we believe are best suited for making claims about detectability, are the γ -models: γA_1 - γD_1 and γA_2 - γD_2 . Here we add grey γ -ray transport sourced by the fraction of nuclear heating that is radiated in the form of γ -radiation (see Sect. 2.2 for details). The letters A-D in the model notation stand for the four different dynamical ejecta morphologies used. Shown in Fig. 19, the light curves for models Xnh₁ and Xnh₂ are nearly identical to those of the γA^* models. This indicates the ray-trace calculation of the γ -thermalization fractions accurately estimate the energy deposition relative to the Monte Carlo model. For this

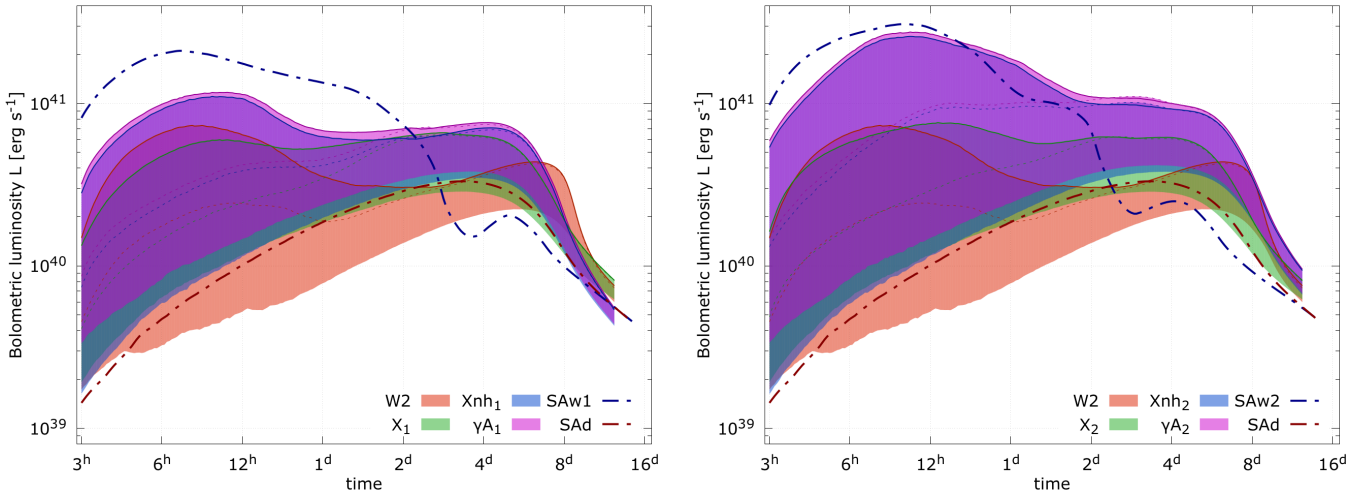


Figure 19. Viewing angle-dependent ranges of bolometric luminosities for the models with detailed heating and thermalization: Xnh_1 , γA_1 (left), and Xnh_2 , γA_2 (right). For comparison, also shown are models having the same composition but with analytic heating, X_1 (left) and X_2 (right), an axisymmetric Zr/Sm model W2, and 1D models with dynamical ejecta mixture opacity SAAd and two types of wind mixed opacities SAw1 (left) and SAw2 (right). Solid lines on the upper edge of each range correspond to the "bottom" orientation of the remnant, and dashed lines of corresponding color indicate bolometric luminosities for the "top" orientation.

reason, the detection prospects of models Xnh_1 and Xnh_2 will be nearly identical to those of models γA_1 and γA_2 , respectively.

The second half of Table 6 contains parameters of these models and their peak bolometric luminosities, for the blue and nIR peaks, for two opposite on-axis remnant orientations, "top" and "bottom". Just as for the W2* models, visibility of the blue peak completely depends on the dynamical ejecta configuration. In particular, models based on dynamical ejecta configuration A (X^* and γA^*) feature the blue peak in both orientations, models based on configurations B and D do not have any, whereas γC_1 and γC_2 have it in the "top" orientation but not in the "bottom" one.

Figure 19 demonstrates bolometric luminosity ranges for the models based on dynamical ejecta configuration A. The upper edge of each range corresponds to the "bottom" orientation, the lower edge is the "side", and the "top" orientation is shown with dashed lines. Thick dot-dashed blue and red lines represent corresponding 1D analytic models SAw1/SAw2 and SAAd, which use wind or dynamical ejecta opacity mix. The light curves of the 2D models lie roughly in between these two extreme cases: they are brighter than the dynamical ejecta-only model SAAd and dimmer than the corresponding model of the wind, SAw1 or SAw2. Model W2 is also shown. It is based on Sm, which has higher opacity than the dynamical ejecta mix that we use, therefore the light curve of W2 is slightly dimmer and peaks later, although the qualitative behaviour is the same.

While models X_1 and X_2 look very similar, once detailed nuclear heating with thermalization is added, not only do they become brighter, model Xnh_2 significantly exceeds Xnh_1 in peak luminosity. This is simply a manifestation of the higher radioactive heating rate for the "wind 2" than for the "wind 1" (shown in Fig. 4, bottom panel). Finally, adding grey γ -transport increases luminosity only marginally. This slight increase is due to the grey γ -transport accounting for nonlocal deposition (from the fraction of energy that escapes each cell), which is not accounted for in our implementation of the thermalization fraction for γ -rays.

The evolution of spectra and light curves for the X^* -models and γ -models is qualitatively similar to that of model W2 (see Fig. 17 and Fig. 18).

For reference, Tables B2, B3, and B4 contain detailed information on the peak magnitudes, epochs and transient durations for all optical and nIR bands, and for the three orientations: top, bottom and side respectively.

5 DETECTION PROSPECTS

In this section, we will focus on our most sophisticated γ -models (see Table 3), and the most promising DZ-models, in which the nuclear heating rates from the FRDM mass model are –for the dynamic ejecta– multiplied by a factor of 10 to mimic the more optimistic Duflo-Zuker heating rates (see Sect. 4).

We adopt methodology of estimating the number of potentially observable macronovae similar to the one in Rosswog et al. (2017), by integrating the expected NSM rate \mathcal{R}_{NSM} over the comoving volume in which the macronova is observable. The only difference is that we also take into account orientation with respect to a terrestrial observer, by weighing the integrand with the probability of favorable orientation $P(z)$:

$$\mathcal{N}_{\text{MN}} = \int \frac{dN}{dz} dz = \mathcal{R}_{\text{NSM}} \int P(z) \frac{dV_C}{dz} \frac{dz}{1+z}, \quad (36)$$

where V_C is the comoving volume. Following Rosswog et al. (2017), we calculate the limiting magnitudes for LSST and VISTA surveys in *grizy* and *JH* bands, respectively, with two exposure times: 60 and 180 seconds, using the same tools (ESO Infrared Exposure Time Calculator for VISTA⁴ and a Python exposure time calculator for LSST⁵, assuming a target signal-to-noise ratio of 5). For the derivative dV_C/dz of the comoving volume with respect to the redshift, we adopt the flat cosmology parameters $H_o = 67 \text{ km s}^{-1} \text{ Mpc}^{-1}$, $\Omega_m = 0.307$ (Planck Collaboration et al. 2016).

The NSM rate that we use to normalize our results (same as in Rosswog et al. 2017) is an "informed best guess" of $\mathcal{R}_{\text{NSM}} =$

⁴ <https://www.eso.org/observing/etc/>

⁵ <https://github.com/lsst-sims/exposure-time-calc>

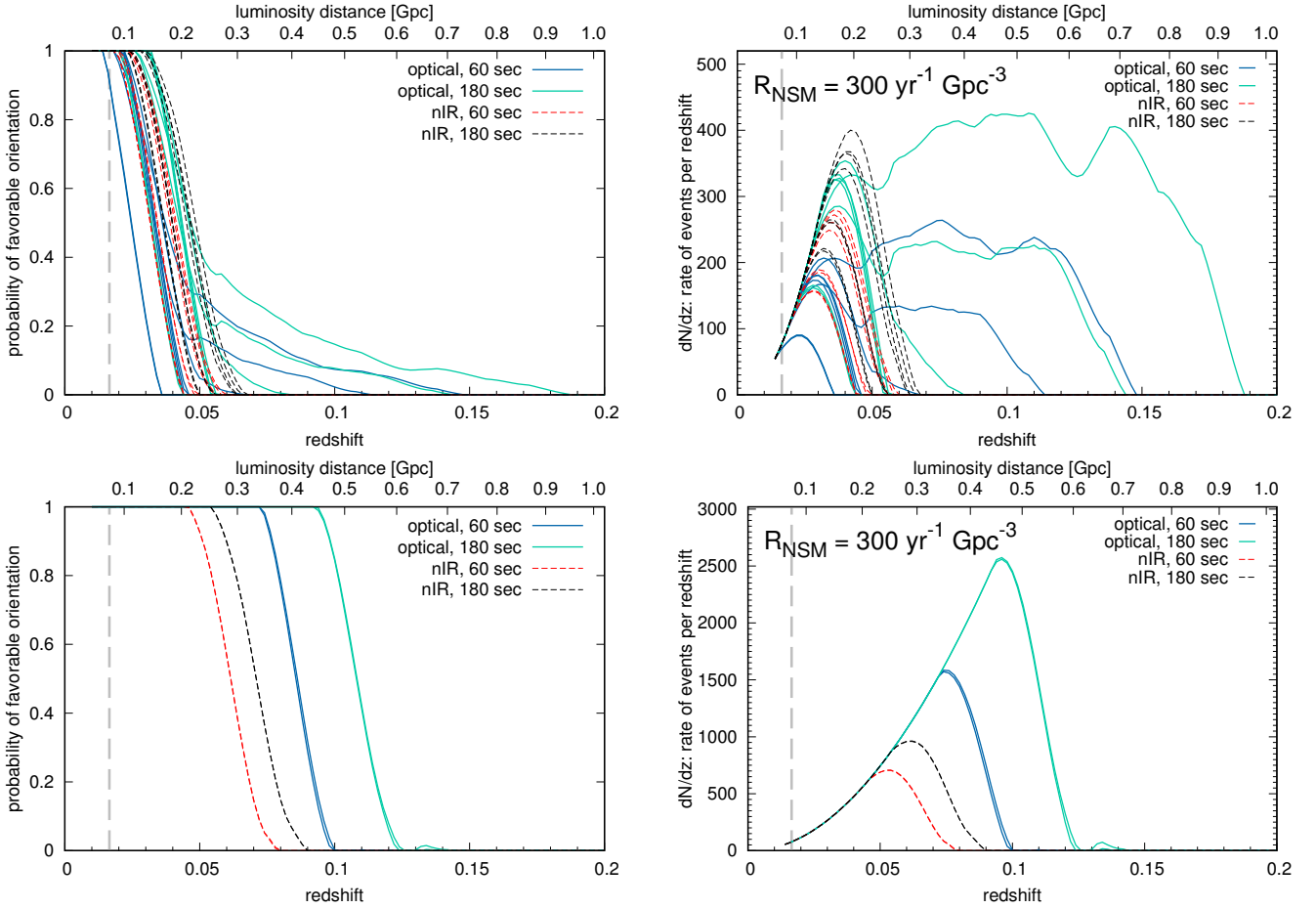


Figure 20. Left: probability of a macronova remnant being oriented such that it can be observed at peak, in the optical or nIR bands, for exposure times 60 and 180 seconds. Right: rate of detectable events per redshift dN/dz , assuming constant volumetric NSM rate of $300 \text{ yr}^{-1} \text{ Gpc}^{-3}$, for optical or nIR bands, and for exposure times of 60 and 180 seconds. The integral under each curve gives the total number of detectable events. Top row: our most realistic γ -models, bottom row: DZ-models with nuclear heating artificially enhanced by a factor of 10. Among the γ -models in the top row, three models stand out: γA_2 , γA_1 and γC_2 . They have a long “tail” of nonzero detection probability in the optical at $z > 0.07$. The grey dashed vertical line corresponds to the aLIGO detection horizon for NSM events for the O1 observing run (about 75 Mpc, Martynov et al. 2016).

$300 \text{ yr}^{-1} \text{ Gpc}^{-3}$, or 25.86 Myr^{-1} per Milky Way size galaxy (assuming 11.6 million Milky Way-equivalent galaxies per Gpc^3). Note that since (36) depends linearly on \mathcal{R}_{NSM} , it is trivial to rescale our results to a different rate. Our choice of this rate value is very conservatively above the expected upper limit for the aLIGO future observation run O3 (Abbott et al. 2016b), to give us room for discussing the prospects of follow-up observations after a future GW trigger. This rate value is also the median (in log scale) of the aLIGO compendium of NSM rates (Abadie et al. 2010), as illustrated by Fig. 2 in Rosswog et al. (2017). It is consistent with the revised NSM rate from the galactic binary pulsar ($7 - 49 \text{ Myr}^{-1}$, Kim et al. 2015), somewhat on the higher end of the rates computed in de Mink & Belczynski (2015) ($1.4 - 81 \text{ Myr}^{-1}$) and used in Belczynski et al. (2016) ($5 - 15 \text{ Myr}^{-1}$) for comparison with LIGO/Virgo upper limits, $0.06 - 77.4 \text{ Myr}^{-1}$ in Dominik et al. (2012) and $0.01 - 80 \text{ Myr}^{-1}$ in Fryer et al. (1999). At the same time, these rates are on the lower side of the rates derived from

models of short GRBs: about $8 - 96 \text{ Myr}^{-1}$ in Fong et al. (2012), and about $43 - 130 \text{ Myr}^{-1}$ in Petrillo et al. (2013)⁶

We compute the probability of favorable orientation $P(z)$ as a ratio of the number of angular bins for which the macronova magnitude is above detection threshold, to the total number of angular bins. Fig. 20, left column, shows $P(z)$ computed for each of the models at peak magnitude using exposure thresholds for 60 and 180 seconds. Since the behaviour of the macronova in the optical and nIR bands is different, we estimate optical and nIR detection probabilities separately. Optical detection probability is taken as the maximum probability over *grizy* bands, and nIR detection probability is the maximum over the *JK* bands.

As can be seen from Fig. 20, $P(z)$ for all our γ -models in the infrared looks rather similar: it is 100% up to about 100 Mpc, then steeply drops to zero, such that none of the models is detectable at redshifts higher than ~ 0.07 . The steep decrease in probability for the two DZ models is qualitatively similar, except they are detectable from farther out, about 300 Mpc. This behavior is due to the fact that even

⁶ But see Guetta & Piran (2005), where pre-SWIFT estimates of short GRBs statistics were used to infer rates as low as $\sim 0.1 \text{ Myr}^{-1}$

Table 7. Total number of observable events across the whole sky, in nIR or optical bands, with exposure times 60 and 180 s, sampled at peak t_p , and at 1 day and 2 days after the merger. Scaled to the NSM rate of $300 \text{ yr}^{-1} \text{ Gpc}^{-3}$ ($\approx 25.86 \text{ Myr}^{-1}$ per Milky Way size galaxy). High-latitude angles where afterglow may be detectable, are not excluded.

Model	nIR (VISTA)		optical (LSST), 60 s			optical (LSST), 180 s		
	60 s	180 s	t_p	1d	2d	t_p	1d	2d
γA_1	3.8	5.8	12.4	5.5	2.1	27.1	12.0	4.5
γA_2	4.9	7.5	27.8	25.2	8.2	59.2	54.6	17.8
γB_1	3.8	5.9	1.8	0.9	0.1	3.9	1.8	0.5
γB_2	4.9	7.5	1.9	1.0	0.4	4.0	2.0	0.9
γC_1	7.1	10.9	4.5	3.9	1.5	9.5	8.4	3.1
γC_2	8.1	12.2	6.1	5.4	3.0	12.8	11.6	6.4
γD_1	7.5	11.7	4.2	3.6	1.2	9.0	7.5	2.5
γD_2	8.4	13.4	4.4	3.8	1.6	9.3	8.0	3.1
DZ ₁	24.8	38.2	65.3	57.5	49.4	130.1	118.6	98.2
DZ ₂	25.0	38.1	66.7	60.6	49.5	131.9	119.7	97.7

though the macronovae are brighter in nIR than in optical, detection thresholds are also much higher. Since macronovae light curves in nIR vary little with orientation – only within a factor of $\sim 2 - 3$, corresponding to about 1 mag – the cutoff to zero is very steep.

In optical, $P(z)$ behaves rather differently, because the flux in optical bands varies by several orders of magnitude depending on the orientation. Three models in Fig. 20 (top left) stand out as detectable to much higher redshifts: with exposure of 180 seconds, γA_2 is visible up to $z = 0.2$, γA_1 up to $z = 0.15$, and γC_2 – up to 0.08. Visibility horizon for exposure of 60 seconds is not much smaller: $z = 0.15$ for γA_2 and $z = 0.11$ for γA_1 . For the two DZ models with enhanced heating rates (bottom left), $P(z)$ is shifted to higher redshifts, because these models produce much brighter optical transients.

The right column in Fig. 20 displays the differential quantity dN/dz from the first integral in (36), which describes the rates of detectable macronovae per redshift. The integral under each of the curves gives estimates of total number of detections, for an assumed rate \mathcal{R}_{NSM} . This plot illustrates that even though the probability of favorable orientation at higher redshifts is small, the majority of detections will be at higher redshifts due to rapidly increasing comoving volume element.

The grey dashed vertical line in Fig. 20 indicates the aLIGO detection horizon for NSM events (75 Mpc, Martynov et al. 2016), computed for the first aLIGO run O1. At such distance, all our models are above detection threshold, both in optical and in nIR, independent of orientation. For subsequent runs the detection horizon is pushed to 200 Mpc, where only a fraction of macronovae is observable. For more distant aLIGO horizon, say 400 Mpc, the majority of NSM GW signals will be unobservable in either nIR or optical bands, at least in surveys with 60/180-second exposure times.

Another factor which complicates the observability of macronovae is their short duration in optical bands. In nIR, this is not such a big problem, because peak times and durations are the order of a week. Fig. 20 shows only the most optimistic probabilities for detections at peak times. If an observation is made several days after the GW trigger, the macronova can be a few mags dimmer. Fig. 18, four top panels, shows a drop by 4 mags in r , i and z bands for model W2 in its favorable on-axis orientation.

Table 7 displays the expected number of potentially observable events for each model, either in nIR (for VISTA) or optical (for LSST), depending on the exposure time and the epoch. The " t_p " columns for optical observations correspond to the peak epochs, and "1d" and "2d" correspond to the observation epochs of one and

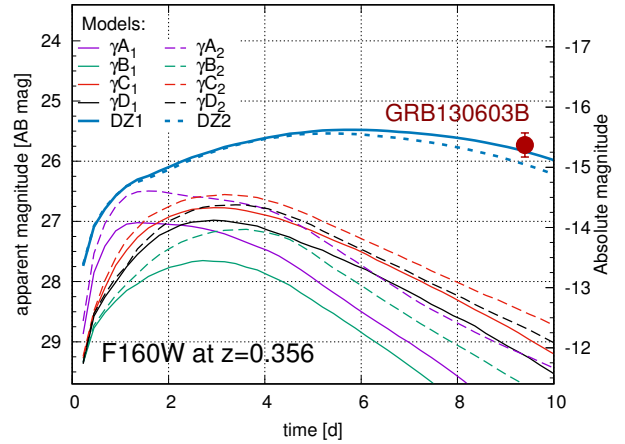


Figure 21. Synthetic light curves from our models, calculated with the F160W filter at redshift $z = 0.356$, corresponding to the distance to GRB130603B. The red circle with error bars indicates the measured nIR excess, interpreted as a kilonova (Tanvir et al. 2013).

two days after the initial trigger, respectively. We can see from the table that observing at one (two) day(s) after the trigger decimates the number of events by a factor of about two (four). One should also take into account that these numbers are for the entire sky, but only a small patch of it will be accessible to generic surveys with high enough cadence.

We could approach the LSST detection rates from another angle, where we start from the supernova detection rate estimates (e.g. Lien & Fields 2009; LSST Science Collaboration et al. 2009). Specifically, for core-collapse supernovae, LSST is estimated to detect as many as 3.43×10^5 events per year (Lien & Fields 2009, Table 2). Our peaks are typically 3-5 magnitudes lower than core collapse supernovae, which translates into rates of 0.4-6.3 detections per year, if we assume that NSMs are ~ 1000 times more rare and that all of them have a blue transient. However, we also need to consider that only one detection epoch will be possible with the LSST observing strategy. Thus, it would seem that the identification of macronovae requires follow-up observations with other telescopes. In this case, their reaction times can be as crucial as for the GW triggers Abbott et al. (2016a) due to the short duration of the blue transients.

One concern for the prospects of macronova detections is that it can be "drowned" in the afterglow from a GRB. However, firstly, not all NSMs do necessarily produce GRBs, because the wind from hypermassive neutron star can create a baryon-polluted cloud around the engine, dense enough to prevent a GRB jet from getting out (Murguia-Berthier et al. 2014; Just et al. 2016) or reaching ultrarelativistic speeds. Secondly, afterglows are only visible from very narrow opening angles, ($< 10^\circ$, Fong et al. 2012), while optical macronovae for our models are visible from much wider angles. In fact, in our numerical setting, where we cover 4π with 27 axisymmetric angular bins equally spaced in $\cos \theta$ (see Sect. 2.3.1), the 10° solid angle only covers $\sim 1/5$ of one polar bin. Thus, our results for optical detection are not affected by the invisibility due to the afterglow.

Can our models explain the observed nIR excess in GRB130603B, which was reported in Tanvir et al. (2013) and de Ugarte Postigo et al. (2014) (also Berger et al. 2013)? Fig. 21 shows the light curves in the F160W band for our most sophisticated γ -models, and the two DZ-models with artificially enhanced nuclear heating

rates, compared with the detection data point. In all γ -models, the FRDM nuclear mass model is used, while DZ models are intended to mimic the Duflo-Zucker DZ31 model (Wu et al. 2016; Rosswog et al. 2017). Nuclear heating rates in the latter are higher than in the former by almost one order of magnitude. While DZ31-based models seem to have no problems reaching the observed brightness, none of the γ -models is even close to the detection.

Moreover, some experimentation shows that no reasonable increase in the ejecta mass or velocity, or wind mass or velocity, can possibly make FRDM-based light curves agree with the GRB130603B observation. At the same time, DZ31-based models explains it with ease. Thus, among other factors, the dominant impact of nuclear heating rate is established. This is already hinted by the scaling expression for bolometric luminosity (28): while other parameters such as ejecta mass, velocity or even opacity enter this expression with powers less than one, nuclear heating is directly proportional to the luminosity. We conclude that future reliable macronova observations will constrain nuclear heating rates in the first place, and so indirectly help discriminating between nuclear mass models.

6 DISCUSSION AND CONCLUSION

We apply the multi-dimensional, multigroup Monte Carlo code SuperNu (Wollaeger & van Rossum 2014) and detailed opacities from the LANL suite of atomic physics codes (Fontes et al. 2015b) to simulate radiative transfer for a series of spherically-symmetric and axisymmetric macronova models and produce light curves and spectra. To demonstrate the accuracy and consistency of our code, we develop a new analytic solution for macronovae (see Appendix A) with uniform homologously expanding background flow and grey opacity treatment. This solution is then simulated with SuperNu in spherical symmetry with full multi-group opacity treatment (see Sect. 2.3.1). For the nuclear heating, which supplies radiative power of the macronova, we use WinNET nuclear network (Winteler 2012; Winteler et al. 2012) to calculate the r -process nucleosynthesis and partitioning of released energy between different decay products.

We systematically explore a series of models with varying level of detail in the morphology, composition, and opacity to understand and disentangle various factors affecting macronova light curves and spectra. We consider two types of outflows: dynamical ejecta and winds, and combine them in our models (see Fig. 1). Morphology is taken from 1D-spherically or 2D-axisymmetrically averaged ejecta from sophisticated 3D SPH Newtonian simulations of neutron star mergers (NSMs, Rosswog et al. 2014). We also develop a new 1D analytic spherically-symmetric hydrodynamic solution to model homologous expansion of the ejecta (Sect. 2.1.1).

For the UV/optical/IR absorption opacity, we explore a range of options: effective grey, detailed for single elements, or detailed for multiple elements with partial density weighted mixing. Our final, most sophisticated models combine 2D dynamical ejecta from NSM simulations with a spherical analytic wind solution, mixed composition opacity, detailed r -process heating from nucleosynthesis network, partitioning of the heating rates between decay products, and individual thermalization of different decay products (following the approach of Barnes et al. 2016). As in the work of Fontes et al. (2017), we use a novel approach in which we depart from the traditional Sobolev treatment of opacity during radiative transfer, and instead use alternative multigroup with “smeared” lines.

For each simulation, Table 3 gives the relevant section and model parameters. Tables 4, 5, 6, give model parameters and peak bolometric luminosity (including time of peak) for the models with

semi-analytic ejecta, averaged SPH ejecta, and dynamical ejecta combined with wind, respectively. Absolute peak magnitudes, peak times, and macronova durations (defined as times to decrease one mag after peak) are provided for *grizyJHK* broadband filters in Table B1 for all 1D models, and in Tables B2, B3, and B4 for “top”, “bottom”, and “side” views, respectively, of each 2D model. These tables show that opacity has a substantial impact on the luminosity, with lanthanides and actinides contributing to broader, redder light curves relative to the other elements tested.

We use the semi-analytic, grey opacity models to calculate power-law fits of peak bolometric luminosity, peak epoch, and peak broadband luminosity with respect to: ejecta mass, median velocity, and opacity. These relationships are given in Sect. 3.1. The scaling relations from our grey opacity models can be used for models with detailed opacity in cases when the spectrum is close to Planckian. For the set of semi-analytic ejecta models, we compare light curves from simulations with grey opacity to light curves from simulations with detailed opacity (see Fig. 11). These comparisons indicate that lanthanide opacities, representative of dynamical ejecta, give peak bolometric luminosities consistent with an effective grey opacity of $\sim 10 \text{ cm}^2 \text{ g}^{-1}$, while lighter element wind-type opacities are consistent with an effective grey opacity closer to $\sim 1 \text{ cm}^2 \text{ g}^{-1}$, justifying the values that had been used in earlier work (Kasen et al. 2013; Tanaka & Hotokezaka 2013; Grossman et al. 2014). However, in the optical and J bands, the effective grey lanthanide opacity significantly overestimates macronova emission (see Fig. 15), while for the H and K bands it gives a reasonable approximation.

We summarize our main findings below, with sections divided according to what features we examine in this study.

6.1 Effect of geometry

The impact of varying ejecta morphology on light curves and spectra, discussed in Sect. 3.3, is largely consistent with our expectations. For the same compositions, the 1D semi-analytic models (presented in Sect. 3.1 and 3.2) produce comparable light curves to the 1D spherically symmetric averages of the SPH ejecta. Moreover, these 1D results fall in between the brightest (top) and dimmest (side) views of the equivalent 2D axisymmetric models. In particular, the broadband data in Table B1 and the bolometric luminosities shown in Fig. 14 of models SASm, A1dSm and B1dSm, show similar transients. The similarity arises from the comparable density profiles, mass, and velocity of the ejecta (see Fig. 2). SASm has the analytic ansatz, and A1dSm and B1dSm have 1D spherically averaged model A and model B SPH ejecta, respectively, as described in Sect. 2.1. Also in Fig. 14 is a plot of the light curve for the 2D model A2dSm at different viewing angles, showing SASm falling between the light curves in the top (or bottom) and side views.

Even without a wind component superimposed, the 2D axisymmetric models produce brighter and bluer transients at top and bottom (or axial) views. The brightness in the top and bottom views is a geometric effect, since a larger projected area of the ejecta photosphere is visible relative to the side views. We find that the transients appear bluer from the top and bottom views because the optical depths from points on the equatorial (merger) plane to the surface are generally lower. Photons can reach the void above or below the merger plane more easily. Consequently, early emission at higher temperature is suppressed less, relative to side views. Generally, morphologies that are non-spherical permit views with bluer and brighter transients, relative to spherical morphologies. For our models, the brightness varies by a factor of 2-3 between side and top viewing angles, consistent with previous work (see, for instance, Grossman et al. 2014).

6.2 Effect of composition

In Section 3.2, we test the effect of opacity for pure elements and mixtures of elements on the light curves and spectra, for a fixed spherically-symmetric ejecta morphology. We find that the brightness and timescale of the transients strongly depends on the atomic electron configurations available to each element in the macronova density-temperature regimes. Specifically, for the set of elements we examine, we find the broadband light curves can be categorized into three distinct types: bright blue transients peaking in a few hours, intermediate red transients with double peaks over 1-2 days (in the *izy* bands), and late nIR transients spanning a week (in the *HK* bands). The blue, red, and nIR transients correspond to opacity from elements with open *p*-shells, *d*-shells, and *f*-shells, respectively. Figures 13 and 12 show the spectra at different times for each model discussed in Sect. 3.2. The spectra from models with mixed composition are dominated by the features from elements that have the most complex electronic configurations of their outer atomic shell, because these tend to contribute the most opacity (as in the findings of Kasen et al. (2013)). These broadband light curve features may be useful in characterizing the composition of dominant sources of opacity in macronova ejecta. However, the detectability of a transient from the wind relies substantially on the composition; a time scale of several hours is not easily amenable to detection in either follow-up or blind surveys (Grossman et al. 2014).

The spectra of dynamical ejecta at late times most closely resemble those of the *f*-shell elements –lanthanides and actinides– and feature a peculiar "spectral cliff", where emission is very strongly suppressed past certain wavelength (for instance, about 1.6 microns for Sm, right in the middle of the H band). Compared to grey opacity models, this leads to much dimmer transients in the optical and J bands, while light curves in the HK bands retain comparable brightness. This can serve as a justification for using simple models for estimating the brightness in the HK bands.

6.3 Effect of "lanthanide curtain"

In Sections 3.4 and 4, we combine the axisymmetric dynamical ejecta from NSM models A-D with various wind model ejecta derived from the 1D analytic solution (presented in Sect. 2.1; see Fig. 1). The combined models assess the visibility of potential blue transients for our various types wind and dynamical ejecta. These models are listed in Table 6.

Figure 16 shows the presence of a blue transient for several of the combined models that employ model A dynamical ejecta. The appearance of the blue transient is orientation-dependent (shown by the shaded regions for the 2D models in Fig. 16). This result is exhibited by the 2D combined mixed composition models as well, seen in Fig. 19.

In more than half of the models in Table 6, the irregular morphology of the ejecta completely or substantially obscures the blue transient in one on-axis view, relative to the other. The dynamical ejecta is not completely symmetric when reflected through the equatorial (merger) plane. The sensitivity of the wind transient to small differences in dynamical ejecta show the impact of lanthanide opacity in these regions. This sensitivity propagates to the detection prospects, shown in Fig. 20. This "lanthanide curtain" has been found in other studies as well (Barnes & Kasen 2013; Kasen et al. 2015).

6.4 Effect of nuclear heating rate

Of the set of macronova properties we explore, the nuclear heating rate has the largest impact on luminosity. As noted in Sect. 5, this is implied by the the exponents of ejecta mass, velocity, and opacity in the power-law scaling relations discussed in Sect. 3.1, which are less than one. Luminosity scales directly proportional to the heating rate, which is implied by the result in Appendix A. Our DZ-model light curves, when compared with the models that use FRDM, indicate that reliable macronova observations will constrain the nuclear heating rates and therefore nuclear physics far from stability. As a corollary, the thermalization efficiencies of the different heating products should have a significant impact on brightness as well, as originally found in the work of Barnes et al. (2016). However, the uncertainty in thermalization efficiency is subdominant compared to the uncertainty in the nuclear heating rate due to the unknown nuclear mass model (also shown in Barnes et al. 2016).

6.5 Detection Prospects

In Section 5, we discuss the detection prospects for our most detailed models: γA_1 , γA_2 , γB_1 , γB_2 , γC_1 , γC_2 , γD_1 , and γD_2 . These models employ detailed r-process heating rates from WinNET, and have a grey multidimensional Monte Carlo energy deposition model for the γ -rays. The models all have assumed the FRDM nuclear mass model for the r-process. Consequently, in this section we also assess the detection prospects for models DZ₁ and DZ₂, which apply the analytic power-law heating, Eq. 18, but multiplied by a factor of 10 in the dynamical ejecta. The increase of the dynamical ejecta heating rate in the DZ-models substantially brightens the light curve in the nIR bands. In particular, for the F160W filter, the light curves for the DZ-models come much closer to the GRB130603B data point than all other models (see Fig. 21). Models with nuclear heating rates similar to what is delivered by the DZ-mass models are consistent with the transient observed in the context of GRB130603B being a macronova.

In Fig. 20 we plot detection probabilities and detection rates per redshift for two exposure times from the LSST (*grizy* bands) and VISTA (*JK* bands) surveys. These values were calculated for each model, assuming an NSM rate of $300 \text{ yr}^{-1} \text{ Gpc}^{-3}$, perfect telescope coverage across the whole sky, and that the model represents all macronovae. The probability of detection is 100 % up to about 100 Mpc for γ -models, and up to 200 Mpc for DZ-models, making them detectable for all events within the LIGO horizon, both in the optical and in the JK bands. A follow-up search is therefore possible, with the infrared bands looking more promising, both due to the longer duration of the transients, and low sensitivity to the orientation.

Only three of the γ -models, which have blue transients that are not fully suppressed by lanthanide curtaining, are detectable at $z > 0.07$. The detection probability decreases at higher redshift until only the view close to the merger axis permits detection of the blue transient. The non-monotonicity of the detection rate per redshift shows the competing effects of increasing NSM sample volume while decreasing apparent magnitude. In the span of redshift where the models are visible in all orientations, the rate of detections per redshift steadily increases. However, once the redshift is sufficiently high, apparent magnitudes are too dim, and the detection rates drop off unless there is a sufficiently bright blue transient from the wind. For the DZ-models, the brighter transients increase the detection prospects substantially past $z = 0.07$. Since the DZ-models only increase the heating in the dynamical ejecta, these models do not

exhibit the same level of anisotropy for the blue transient and hence do not have prominent tails in the probability for optical detections. In Table 7, we have integrated the detection rate per redshift with respect to redshift to get total (ideal) detection rates for each model and each exposure. Consequently, the assumed NSM rate of $300 \text{ yr}^{-1} \text{ Gpc}^{-3}$ applies to these numbers as well (they can be multiplicatively rescaled to a different NSM rate). Generally, for the γ -models, we find O(1-10) detections are possible per year, assuming total coverage of the sky at all times. For the DZ models, we find O(10-100) possible detections, again under the same assumptions. The difference in the ideal detection rate between the γ -models and the DZ-models is consistent with the difference in the heating rates for the models.

6.6 Comparison with other macronova studies

It is difficult to make precise comparisons with the existing macronova literature, given the differences in ejecta morphologies, r-process heating models, and assumed compositions.

First studies of macronovae (e.g. Li & Paczyński 1998; Roberts et al. 2011) estimated ejecta opacities to be similar to the opacity of nickel ($0.2 \text{ cm}^2 \text{ g}^{-1}$) which was proven to be overly optimistic (Kasen et al. 2013). Such high opacities led to the bolometric luminosities in the range of $\sim 10^{42} - 10^{44} \text{ erg s}^{-1}$ (Fig. 2 of Li & Paczyński (1998)), on par with supernovae and much brighter than all of our models. Roberts et al. (2011) performed full radiative transfer on multidimensional ejecta, but applied a constant grey opacity of $0.1 \text{ cm}^2/\text{g}$. Consequently, their peak bolometric luminosities are $\sim 10^{42} \text{ erg s}^{-1}$ as well⁷. The work of Barnes & Kasen (2013), Tanaka & Hotokezaka (2013), Kasen et al. (2013), and Grossman et al. (2014), use opacity that should be more representative of r-process ejecta. These studies report peak bolometric luminosities in the range of $\sim 10^{40} - 10^{41} \text{ erg/s}$. The recent work of Barnes et al. (2016) on thermalization fractions further dims the transient, to a few times 10^{40} erg/s for their fiducial model ($M_{\text{ej}} = 5 \times 10^{-3} M_{\odot}$, $v_{\text{ej}} = 0.2c$). In general, for emission from the dynamical ejecta, the bolometric luminosities of our models are a few times 10^{40} erg/s . Recently, Fontes et al. (2015a) and Fontes et al. (2017) applied a line-smearing multigroup approach in LTE light curve calculations, which is the method we apply for opacity in this work (albeit, with a different treatment of relativistic transformations). Our luminosities in the mid-IR range are $\sim 10^{40} \text{ erg/s}$ for dynamical ejecta without wind, consistent with the findings of Fontes et al. (2015a, 2017). In comparison with Rosswog et al. (2017), our models are similar in absolute brightness but differ by having much shorter durations in the optical *grizy* bands (as can be seen in Fig. 18) making them much harder to detect for LSST. This is due to the differences between the wind mass adopted in our models; otherwise, the grey opacity of $\kappa = 1 \text{ cm}^2 \text{ g}^{-1}$ gives a reasonable agreement with our multigroup study (see Sect. 3.2). Moreover, Rosswog et al. (2017) reports absolute brightness of $-15.. -16$ in the *K* band, which is similar to the values obtained in this study (see Tables B2, B3, B4).

6.7 Caveats and Future work

Our results have a number of approximations, both in the underlying numerical methods, and in the problem configurations. For the radiative transfer, SuperNu assumes LTE, which limits the reliability

⁷ If we apply equation (28) to rescale our 1D peak bolometric luminosity to a grey opacity of $0.1 \text{ cm}^2/\text{g}$, the result is $\sim 4.4 \times 10^{41}$.

of the light curves and spectra in the late stages of the expansion of the ejecta. We also do not treat lines directly, but instead apply a multigroup approach that we justify in Sect. 2.3.1. For the opacity, we weight contributions from pure elements by their partial density in the mixed compositions. A more accurate approach would be to solve the Saha-Boltzmann equations (for LTE) for each species, coupled through the free electron field. This would give more accurate ion population densities for the subsequent opacity calculation.

The explored matter configurations are based on essentially Newtonian SPH simulations. Fully relativistic simulations, especially when coupled to a soft nuclear matter equation of state that enhance the likelihood of shocks, may therefore lead to different matter configurations and possibly larger electron fractions. While many of the quantities that are determined by the 'astrophysical engine' at work enter with powers smaller than unity into the observables (such as peak times and luminosities, see Sect. 3.1), the nuclear heating rate impacts the luminosity linearly. It is determined by nuclear physics far from stability which may be decisive for whether macronovae are detectable at interesting rates or not.

7 ACKNOWLEDGMENTS

Work at LANL was done under the auspices of the National Nuclear Security Administration of the U.S. Department of Energy at Los Alamos National Laboratory under Contract No. DE-AC52-06NA25396. All LANL calculations were performed on LANL Institutional Computing resources. SR has been supported by the Swedish Research Council (VR) under grant number 2016-03657_3, by the Swedish National Space Board under grant number Dnr. 107/16 and by the research environment grant "Gravitational Radiation and Electromagnetic Astrophysical Transients (GREAT)" funded by the Swedish Research council (VR) under Dnr 2016-06012. Some of the simulations for this paper were performed on the facilities of the North-German Supercomputing Alliance (HLRN). We thank Mansi Kasliwal for useful input on detection prospects.

APPENDIX A: ANALYTIC MACRONOVA SOLUTION

The analytic solutions obtained for Fig. 5 follow the prescription of Pinto & Eastman (2000). For clarity, we outline the derivation here. The semi-relativistic radiation diffusion equation is

$$\frac{DE}{Dt} - \nabla \cdot \left(\frac{c}{3\kappa\rho} \nabla E \right) + \frac{4}{3} E \nabla \cdot \vec{v} = \rho \dot{\epsilon} \quad , \quad (\text{A1})$$

where t is time, ∇ is the gradient or divergence operator ($\nabla \cdot$) with respect to spatial coordinate \vec{r} , E is comoving radiation energy density, \vec{v} is velocity, c is the speed of light, κ is a constant absorption opacity, ρ is gas density, and $\dot{\epsilon}$ is the radioactive heating rate per unit mass. In Eq. (A1), it has been assumed that the thermal absorption and emission rates cancel. Restricting to 1D spherical geometry, the

supporting equations are

$$\vec{v} = \frac{\vec{r}}{t}, \quad (\text{A2a})$$

$$|\vec{v}| = v = v_{\max} x, \quad (\text{A2b})$$

$$\rho = \rho_0 \left(\frac{t_0}{t}\right)^3, \quad (\text{A2c})$$

$$E = E_0 \left(\frac{t_0}{t}\right)^4 \psi(x)\phi(t), \quad (\text{A2d})$$

$$T = (E/a)^{1/4}, \quad (\text{A2e})$$

$$\dot{\epsilon} = \epsilon_0 t^{-\alpha}, \quad (\text{A2f})$$

where v_{\max} is the maximum outflow speed, x is a non-dimensional radial coordinate, t_0 is an initial time, ρ_0 is density at t_0 , and $\psi(x)$ and $\phi(t)$ are the spatial and temporal profiles of the radiation energy density. Also, T is gas or radiation temperature (a is the radiation constant), and α is a constant taken to be 1.3 for r-process heating. In Eq. (A2), it is assumed the outflow is homologous and the radiation energy density solution is amenable to separation of variables. Using Eq. (A2) to evaluate each term on the left side of Eq. (A1),

$$\frac{DE}{Dt} = E_0 \left(\frac{t_0}{t}\right)^4 \psi(x) \left(\phi'(t) - \frac{4}{t}\phi(t)\right), \quad (\text{A3a})$$

$$-\nabla \cdot \left(\frac{c}{3\kappa\rho} \nabla E\right) = -\frac{1}{(v_{\max}t_0)^2} \left(\frac{t_0}{t}\right) \phi(t) \left(\frac{cE_0}{3\kappa\rho_0}\right) \frac{1}{x^2} \left(x^2\psi'(x)\right)', \quad (\text{A3b})$$

$$\frac{4}{3}E\nabla \cdot \vec{v} = \frac{4}{t}E_0 \left(\frac{t_0}{t}\right)^4 \psi(x)\phi(t). \quad (\text{A3c})$$

Summing Eqs. (A3) and cancelling $(t_0/t)^3$,

$$E_0 \left(\frac{t_0}{t}\right) \psi(x)\phi'(t) - \frac{1}{(v_{\max}t_0)^2} \phi(t) \left(\frac{cE_0}{3\kappa\rho_0}\right) \frac{1}{x^2} \left(x^2\psi'(x)\right)' = \rho_0\epsilon_0 t^{-\alpha}. \quad (\text{A4})$$

The homogeneous form of Eq. (A4) is solved first, allowing separation of variables,

$$\frac{1}{x^2\psi(x)} \left(x^2\psi'(x)\right)' = -\lambda, \quad (\text{A5a})$$

$$\tau_0 \left(\frac{t_0}{t}\right) \frac{\phi'(t)}{\phi(t)} = -\lambda, \quad (\text{A5b})$$

where λ is the separation constant and

$$\tau_0 = \frac{3\kappa\rho_0}{c} (v_{\max}t_0)^2. \quad (\text{A6})$$

The boundary conditions of Eqs. (A5) are

$$\psi(0) = 0, \quad (\text{A7a})$$

$$\psi(x_0) = 0, \quad (\text{A7b})$$

$$\phi(t_0) = 1, \quad (\text{A7c})$$

$$\phi(\infty) = 0. \quad (\text{A7d})$$

The solutions to Eqs. (A5) and (A7) are (Pinto & Eastman 2000)

$$\psi(x) = \frac{\sin(\sqrt{\lambda}x/x_0)}{x}, \quad (\text{A8a})$$

$$\phi_h(t) = \exp(-\lambda t^2/2\tau_0 t_0). \quad (\text{A8b})$$

For optically thick outflow, the radiative-zero boundary condition can reasonably be set as $x_0 = 1$, $\psi(1) = 0$ (Pinto & Eastman 2000). Following Pinto & Eastman (2000), bracket notation will be used for non-dimensional spatial integrals of products of functions:

$$\langle f|g \rangle = \int_0^1 f(x)g(x)x^2 dx. \quad (\text{A9})$$

Requiring

$$\langle \psi|\psi \rangle = 1, \quad (\text{A10})$$

the set of spatial eigenfunctions satisfying the boundary conditions are

$$\psi_m(x) = \sqrt{2} \frac{\sin(m\pi x)}{x}. \quad (\text{A11})$$

Multiplying Eq. (A4) by $\psi_m(x)x^2$ and integrating over $x \in [0, 1]$ yields

$$\phi'_m(t) + \left(\frac{t}{t_0\tau_0}\right) \left(m^2\pi^2\right) \phi_m(t) = \frac{\rho_0}{E_0 t_0} \epsilon_0 t^{1-\alpha} \langle 1|\psi_m \rangle. \quad (\text{A12})$$

It is convenient to rescale the time variables as well:

$$t \rightarrow t_0 t, \quad (\text{A13a})$$

$$\tau_0 \rightarrow t_0 \tau_0, \quad (\text{A13b})$$

$$\frac{\rho_0}{E_0} \epsilon_0 t_0^{1-\alpha} \rightarrow \epsilon_0. \quad (\text{A13c})$$

Substituting Eqs. (A13) into Eq. (A12) yields

$$\phi'_m(t) + \left(\frac{t}{\tau_0}\right) \left(m^2\pi^2\right) \phi_m(t) = \sqrt{2}\epsilon_0 \frac{(-1)^{m+1}}{m\pi} t^{1-\alpha}, \quad (\text{A14})$$

which provides an inhomogeneous temporal eigenfunction. The bolometric luminosity solution is (Pinto & Eastman 2000),

$$L(t) = -\frac{4\pi c U_{\max} t_0 E_0}{3\kappa\rho_0} \sum_{m=1}^{\infty} \phi_m(t) (x^2\psi'_m(x))|_{x=1}. \quad (\text{A15})$$

Incorporating Eqs. (A5a) and (A11) into Eq. (A15),

$$L(t) = \frac{4\pi c U_{\max} t_0 E_0}{3\kappa\rho_0} \sum_{m=1}^{\infty} \phi_m(t) \lambda \langle 1|\psi_m \rangle, \quad (\text{A16})$$

or

$$L(t) = \frac{4\pi c U_{\max} t_0 E_0}{3\kappa\rho_0} \sqrt{2} \sum_{m=1}^{\infty} (-1)^{m+1} m\pi \phi_m(t). \quad (\text{A17})$$

For the test examined in Sect. 2.3, we find the solution is converged at $m \sim 500$.

APPENDIX B: MACRONOVAE: PEAK MAGNITUDES, EPOCHS AND DURATIONS

REFERENCES

- Aasi J., et al., 2014, *ApJS*, 211, 7
- Abadie J., et al., 2010, *Classical and Quantum Gravity*, 27, 173001
- Abbott B. P., et al., 2016a, *ApJ*, 826, L13
- Abbott B. P., et al., 2016b, *ApJ*, 832, L21
- Abdikamalov E., Burrows A., Ott C. D., Löffler F., O'Connor E., Dolence J. C., Schnetter E., 2012, *ApJ*, 755, 111
- Acernese F., et al., 2015, *Classical and Quantum Gravity*, 32, 024001
- Akutsu T., the KAGRA Collaboration 2015, *Journal of Physics Conference Series*, 610, 012016
- Arcones A., Martínez-Pinedo G., 2011, *Phys. Rev. C*, 83, 045809
- Arcones A., Janka H.-T., Scheck L., 2007, *A&A*, 467, 1227
- Barnes J., Kasen D., 2013, *ApJ*, 775, 18
- Barnes J., Kasen D., Wu M.-R., Martínez-Pinedo G., 2016, *ApJ*, 829, 110
- Bartos I., Huard T. L., Márka S., 2016, *ApJ*, 816, 61
- Bauswein A., Goriely S., Janka H.-T., 2013, *ApJ*, 773, 78
- Belczynski K., Repetto S., Holz D. E., O'Shaughnessy R., Bulik T., Berti E., Fryer C., Dominik M., 2016, *ApJ*, 819, 108
- Berger E., 2014, *ARA&A*, 52, 43
- Berger E., Fong W., Chornock R., 2013, *ApJ*, 774, L23
- Blinnikov S. I., Röpke F. K., Sorokina E. I., Gieseler M., Reinecke M., Travaglio C., Hillebrandt W., Stritzinger M., 2006, *A&A*, 453, 229
- Bloom J. S., Sigurdsson S., Pols O. R., 1999, *MNRAS*, 305, 763
- Chen W.-X., Beloborodov A. M., 2007, *ApJ*, 657, 383
- Chu Q., Howell E. J., Rowlinson A., Gao H., Zhang B., Tingay S. J., Boer M., Wen L., 2015, preprint, ([arXiv:1509.06876](https://arxiv.org/abs/1509.06876))
- Ciolfi R., Siegel D. M., 2015, *ApJ*, 798, L36
- Copperwheat C. M., et al., 2016, *MNRAS*, 462, 3528
- Côté B., Belczynski K., Fryer C. L., Ritter C., Paul A., Wehmeyer B., O'Shea B. W., 2017, *ApJ*, 836, 230
- Densmore J. D., Urbatsch T. J., Evans T. M., Buksas M. W., 2007, *Journal of Computational Physics*, 222, 485
- Densmore J. D., Thompson K. G., Urbatsch T. J., 2012, *Journal of Computational Physics*, 231, 6924
- Dessart L., Ott C. D., Burrows A., Rosswog S., Livne E., 2009, *ApJ*, 690, 1681
- Dessart L., Hillier D. J., Woosley S., Livne E., Waldman R., Yoon S.-C., Langer N., 2016, *MNRAS*, 458, 1618
- Doctor Z., et al., 2017, *ApJ*, 837, 57
- Dominik M., Belczynski K., Fryer C., Holz D. E., Berti E., Bulik T., Mandel I., O'Shaughnessy R., 2012, *ApJ*, 759, 52
- Duflo J., Zuker A. P., 1995, *Phys. Rev. C*, 52, R23
- East W. E., Pretorius F., Stephens B. C., 2012, *Phys. Rev. D*, 85, 124009
- Eastman R. G., Pinto P. A., 1993, *ApJ*, 412, 731
- Eichler D., Livio M., Piran T., Schramm D. N., 1989, *Nature*, 340, 126
- Endrizzi A., Ciolfi R., Giacomazzo B., Kastaun W., Kawamura T., 2016, *Classical and Quantum Gravity*, 33, 164001
- Fernández R., Metzger B. D., 2013, *MNRAS*, 435, 502
- Fernández R., Metzger B. D., 2015, preprint, ([arXiv:1512.05435](https://arxiv.org/abs/1512.05435))
- Fernández R., Kasen D., Metzger B. D., Quataert E., 2015, *MNRAS*, 446, 750
- Fernández R., Foucart F., Kasen D., Lippuner J., Desai D., Roberts L. F., 2016, preprint, ([arXiv:1612.04829](https://arxiv.org/abs/1612.04829))
- Fischer T., Whitehouse S. C., Mezzacappa A., Thielemann F.-K., Liebendörfer M., 2010, *A&A*, 517, A80
- Fleck J., Cummings J., 1971, *Journal of Computational Physics*, 8, 313
- Fong W., Berger E., 2013, *ApJ*, 776, 18
- Fong W., et al., 2012, *ApJ*, 756, 189
- Fontes C. J., Fryer C. L., Hungerford A. L., Hakeel P., Colgan J., Kilcrease D. P., Sherrill M. E., 2015a, *High Energy Density Physics*, 16, 53
- Fontes C. J., et al., 2015b, *Journal of Physics B: Atomic, Molecular and Optical Physics*, 48, 144014
- Fontes C. J., Fryer C. L., Hungerford A. L., Wollaeger R. T., Rosswog S., Berger E., 2017, preprint, ([arXiv:1702.02990](https://arxiv.org/abs/1702.02990))
- Foucart F., et al., 2015, *Phys. Rev. D*, 91, 124021
- Foucart F., et al., 2016, preprint, ([arXiv:1611.01159](https://arxiv.org/abs/1611.01159))
- Freiburghaus C., Rosswog S., Thielemann F.-K., 1999, *ApJ*, 525, L121
- Fryer C. L., Woosley S. E., Hartmann D. H., 1999, *ApJ*, 526, 152
- Fryer C. L., Belczynski K., Ramirez-Ruiz E., Rosswog S., Shen G., Steiner A. W., 2015, *ApJ*, 812, 24
- Ghosh S., Bloemen S., Nelemans G., Groot P. J., Price L. R., 2015, preprint, ([arXiv:1511.02673](https://arxiv.org/abs/1511.02673))
- Giacomazzo B., Perna R., Rezzolla L., Troja E., Lazzati D., 2013, *ApJ*, 762, L18
- Gold R., Bernuzzi S., Thierfelder M., Brüggemann B., Pretorius F., 2012, *Phys. Rev. D*, 86, 121501
- Goriely S., Bauswein A., Janka H.-T., 2011, *ApJ*, 738, L32
- Grossman D., Korobkin O., Rosswog S., Piran T., 2014, *MNRAS*, 439, 757
- Guetta D., Piran T., 2005, *A&A*, 435, 421
- Hirai Y., Ishimaru Y., Saitoh T. R., Fujii M. S., Hidaka J., Kajino T., 2015, *ApJ*, 814, 41
- Hotokezaka K., Kiuchi K., Kyutoku K., Okawa H., Sekiguchi Y.-i., Shibata M., Taniguchi K., 2013, *Phys. Rev. D*, 87, 024001
- Hotokezaka K., Wanajo S., Tanaka M., Bamba A., Terada Y., Piran T., 2015a, preprint ([arXiv:1511.05580](https://arxiv.org/abs/1511.05580))
- Hotokezaka K., Piran T., Paul M., 2015b, *Nature*, 11, 1042
- Ji A. P., Frebel A., Chiti A., Simon J. D., 2015, preprint, ([arXiv:1512.01558](https://arxiv.org/abs/1512.01558))
- Jin Z.-P., Li X., Cano Z., Covino S., Fan Y.-Z., Wei D.-M., 2015, *ApJ*, 811, L22
- Just O., Bauswein A., Pulpillo R. A., Goriely S., Janka H.-T., 2015, *MNRAS*, 448, 541
- Just O., Obergaulinger M., Janka H.-T., Bauswein A., Schwarz N., 2016, *ApJ*, 816, L30
- Karp A. H., Lasher G., Chan K. L., Salpeter E. E., 1977, *ApJ*, 214, 161
- Kasen D., Thomas R. C., Nugent P., 2006, *ApJ*, 651, 366
- Kasen D., Badnell N. R., Barnes J., 2013, *ApJ*, 774, 25
- Kasen D., Fernández R., Metzger B. D., 2015, *MNRAS*, 450, 1777
- Kawaguchi K., Kyutoku K., Nakano H., Okawa H., Shibata M., Taniguchi K., 2015, *Phys. Rev. D*, 92, 024014
- Kim C., Perera B. B. P., McLaughlin M. A., 2015, *MNRAS*, 448, 928
- Korobkin O., Rosswog S., Arcones A., Winteler C., 2012, *MNRAS*, 426, 1940
- Kozyreva A., et al., 2017, *MNRAS*, 464, 2854
- Kromer M., Sim S. A., 2009, *MNRAS*, 398, 1809
- Kulkarni S. R., 2005, *ArXiv Astrophysics e-prints*,
- Kyutoku K., Ioka K., Shibata M., 2013, *Phys. Rev. D*, 88, 041503
- Kyutoku K., Ioka K., Okawa H., Shibata M., Taniguchi K., 2015, *Phys. Rev. D*, 92, 044028
- LST Science Collaboration et al., 2009, preprint, ([arXiv:0912.0201](https://arxiv.org/abs/0912.0201))
- Lattimer J. M., Schramm D. N., 1974, *ApJ*, 192, L145
- Lattimer J. M., Mackie F., Ravenhall D. G., Schramm D. N., 1977, *ApJ*, 213, 225
- Lee W. H., Ramirez-Ruiz E., 2007, *New Journal of Physics*, 9, 17
- Lehner L., Liebling S. L., Palenzuela C., Caballero O. L., O'Connor E., Anderson M., Neilsen D., 2016, *Classical and Quantum Gravity*, 33, 184002
- Li L.-X., Paczyński B., 1998, *ApJ*, 507, L59
- Lien A., Fields B. D., 2009, *J. Cosmology Astropart. Phys.*, 1, 047
- Lippuner J., Roberts L. F., 2015, *ApJ*, 815, 82
- Livne E., 1993, *ApJ*, 412, 634
- Martin D., Perego A., Arcones A., Thielemann F.-K., Korobkin O., Rosswog S., 2015, *ApJ*, 813, 2
- Martynov D. V., et al., 2016, *Phys. Rev. D*, 93, 112004
- Mendoza-Temis J. d. J., Wu M.-R., Langanke K., Martínez-Pinedo G., Bauswein A., Janka H.-T., 2015, *Phys. Rev. C*, 92, 055805
- Metzger B. D., 2016, preprint, ([arXiv:1610.09381](https://arxiv.org/abs/1610.09381))
- Metzger B. D., Berger E., 2012, *ApJ*, 746, 48
- Metzger B. D., Fernández R., 2014, *MNRAS*, 441, 3444
- Metzger B. D., Piro A. L., Quataert E., 2008, *MNRAS*, 390, 781
- Metzger B. D., et al., 2010, *MNRAS*, 406, 2650
- Möller P., Nix J. R., Myers W. D., Swiatecki W. J., 1995, *Atomic Data and Nuclear Data Tables*, 59, 185
- Murguía-Berthier A., Montes G., Ramirez-Ruiz E., De Colle F., Lee W. H., 2014, *ApJ*, 788, L8

- Nakar E., 2007, *Phys. Rep.*, 442, 166
- Nissanke S., Kasliwal M., Georgieva A., 2013, *ApJ*, 767, 124
- Noebauer U. M., Sim S. A., Kromer M., Röpke F. K., Hillebrandt W., 2012, *MNRAS*, 425, 1430
- Panov I. V., Kolbe E., Pfeiffer B., Rauscher T., Kratz K.-L., Thielemann F.-K., 2005, *Nuclear Physics A*, 747, 633
- Panov I. V., Korneev I. Y., Rauscher T., Martínez-Pinedo G., Kelić-Heil A., Zinner N. T., Thielemann F.-K., 2010, *A&A*, 513, A61
- Perego A., Rosswog S., Cabezón R. M., Korobkin O., Käppeli R., Arcones A., Liebendörfer M., 2014, *MNRAS*, 443, 3134
- Petrillo C. E., Dietz A., Cavaglià M., 2013, *ApJ*, 767, 140
- Pinto P. A., Eastman R. G., 2000, *ApJ*, 530, 744
- Piran T., 2005, *Rev. Mod. Phys.*, 76, 1143
- Piran T., Nakar E., Rosswog S., 2013, *MNRAS*, 430, 2121
- Planck Collaboration et al., 2016, *A&A*, 594, A13
- Popham R., Woosley S. E., Fryer C., 1999, *ApJ*, 518, 356
- Radice D., Galeazzi F., Lippuner J., Roberts L. F., Ott C. D., Rezzolla L., 2016, *MNRAS*, 460, 3255
- Rauscher T., Thielemann F.-K., 2000, *Atomic Data and Nuclear Data Tables*, 75, 1
- Roberts L. F., Woosley S. E., Hoffman R. D., 2010, *ApJ*, 722, 954
- Roberts L. F., Kasen D., Lee W. H., Ramirez-Ruiz E., 2011, *ApJ*, 736, L21
- Rosswog S., 2005, *ApJ*, 634, 1202
- Rosswog S., 2013, *Philosophical Transactions of the Royal Society of London Series A*, 371, 20272
- Rosswog S., 2015a, *Living Reviews in Computational Astrophysics*, 1, 1
- Rosswog S., 2015b, *International Journal of Modern Physics D*, 24, 30012
- Rosswog S., Liebendörfer M., 2003, *MNRAS*, 342, 673
- Rosswog S., Price D., 2007, *MNRAS*, 379, 915
- Rosswog S., Liebendörfer M., Thielemann F.-K., Davies M. B., Benz W., Piran T., 1999, *A&A*, 341, 499
- Rosswog S., Davies M. B., Thielemann F.-K., Piran T., 2000, *A&A*, 360, 171
- Rosswog S., Korobkin O., Arcones A., Thielemann F.-K., Piran T., 2014, *MNRAS*, 439, 744
- Rosswog S., Feindt U., Korobkin O., Wu M.-R., Sollerman J., Goobar A., Martínez-Pinedo G., 2017, *Classical and Quantum Gravity*, 34, 104001
- Sekiguchi Y., Kiuchi K., Kyutoku K., Shibata M., Taniguchi K., 2016, *Phys. Rev. D*, 93, 124046
- Shen H., Toki H., Oyamatsu K., Sumiyoshi K., 1998a, *Progress of Theoretical Physics*, 100, 1013
- Shen H., Toki H., Oyamatsu K., Sumiyoshi K., 1998b, *Nuclear Physics, A* 637, 435
- Siegel D. M., Cioffi R., Rezzolla L., 2014, *ApJ*, 785, L6
- Singer L. P., et al., 2014, *ApJ*, 795, 105
- Snedden C., Cowan J. J., Gallino R., 2008, *ARA&A*, 46, 241
- Sobolev V. V., 1960, *Soviet Ast.*, 4, 372
- Sutherland R. S., 1998, *MNRAS*, 300, 321
- Swartz D. A., Sutherland P. G., Harkness R. P., 1995, *ApJ*, 446, 766
- Tanaka M., Hotokezaka K., 2013, *ApJ*, 775, 113
- Tanaka M., Hotokezaka K., Kyutoku K., Wanajo S., Kiuchi K., Sekiguchi Y., Shibata M., 2014, *ApJ*, 780, 31
- Tanvir N. R., Levan A. J., Fruchter A. S., Hjorth J., Hounsell R. A., Wiersema K., Tunnicliffe R. L., 2013, *Nature*, 500, 547
- The LIGO Scientific Collaboration et al., 2015, *Classical and Quantum Gravity*, 32, 074001
- Thielemann F.-K., et al., 2011, *Progress in Particle and Nuclear Physics*, 66, 346
- Turner G., Harrison T. M., Holland G., Mojszsis S. J., Gilmour J., 2004, *Science*, 306, 89
- Verner D. A., Ferland G. J., Korista K. T., Yakovlev D. G., 1996, *ApJ*, 465, 487
- Wallner A., et al., 2015, *Nature Communications*, 6, 5956
- Wanajo S., Sekiguchi Y., Nishimura N., Kiuchi K., Kyutoku K., Shibata M., 2014, *ApJ*, 789, L39
- Winteler C., 2012, PhD thesis, The University of Basel, Basel, Switzerland
- Winteler C., Käppeli R., Perego A., Arcones A., Vasset N., Nishimura N., Liebendörfer M., Thielemann F.-K., 2012, *ApJ*, 750, L22
- Wollaeger R. T., van Rossum D. R., 2014, *ApJS*, 214, 28
- Wollaeger R. T., van Rossum D. R., Graziani C., Couch S. M., Jordan IV G. C., Lamb D. Q., Moses G. A., 2013, *ApJS*, 209, 36
- Wu M.-R., Fernández R., Martínez-Pinedo G., Metzger B. D., 2016, *MNRAS*, 463, 2323
- Yang B., et al., 2015, *Nature Communications*, 6, 7323
- de Mink S. E., Belczynski K., 2015, *ApJ*, 814, 58
- de Ugarte Postigo A., et al., 2014, *A&A*, 563, A62
- van Rossum D. R., 2012, *ApJ*, 756, 31
- van Rossum D. R., Kashyap R., Fisher R., Wollaeger R. T., García-Berro E., Aznar-Siguán G., Ji S., Lorén-Aguilar P., 2016, *ApJ*, 827, 128